Memoirs on Differential Equations and Mathematical Physics
Volume 53, 2010, 63–97

J. Elschner, G. C. Hsiao, and A. Rathsfeld

RECONSTRUCTION OF ELASTIC OBSTACLES FROM THE FAR-FIELD DATA OF SCATTERED ACOUSTIC WAVES

Abstract. We consider the inverse problem for an elastic body emerged in a fluid due to an acoustic wave. The shape of this obstacle is to be reconstructed from the far-field pattern of the scattered wave. For the numerical solution in the two-dimensional case, we compare a simple Newton type iteration method with the Kirsch–Kress algorithm. Our computational tests reveal that the Kirsch–Kress method converges faster for obstacles with very smooth boundaries. The simple Newton method, however, is more stable in the case of not so smooth domains and more robust with respect to measurement errors.

2010 Mathematics Subject Classification. 35R30 76Q05 35J05.

Key words and phrases. Acoustic and elastic waves, inverse scattering, simple Newton iteration, Kirsch–Kress method.

რეზიუმე. ჩვენ განვიხილავთ სითხეში აკუსტიკური ტალღების მოქმედებით ჩაძირული დრეკადი სხეულისთვის დასმულ შებრუნებულ ამოცანას. ამ დაბრკოლების ფორმა აღდგენილი უნდა იქნას გაბნეული ტალღების შორეული ველის მონაცემებით. ორგანზომილებიან შემთხვევაში მარტივი ნიუტონის ტიპის იტერაციით მიღებულ რიცხვით ამონახსნს ვადარებთ კირშ-კრესის ალგორითმით მიღებულ ამონახსნს. ტესტური გამოთვლები გვიჩვენებენ, რომ მაღალი სიგლუვის მქონე საზღვრიანი დაბრკოლებებისათვის კირშ-კრესის მეთოდი უზრუნველყოფს უფრო სწრაფ კრებადობას. მეორეს მხრივ, მარტივი ნიუტონის ტიპის მეთოდი გაცილებით უფრო სტაბილურია იმ შემთხვევაში, როდესაც დაბრკოლების საზღვარს არ გააჩნია მაღალი სიგლუვე, ის აგრეთვე უფრო მდგრადია გაზომვის ცდომილებების მიმართ.

1. Introduction

If an elastic body is subject to an acoustic wave propagating through the surrounding fluid, then an elastic wave is generated inside the body, and the acoustic wave is perturbed (cf. Figure 1). The wave perturbation is characterized by the asymptotics of the scattered field, namely, the far-field pattern. Suppose the material properties of body and surrounding fluid are known. Then the usual inverse problem of obstacle scattering is to determine the shape of the body from measured far-field data generated by plane waves incident from one or from a finite number of directions. This problem is extremely ill-posed such that regularization techniques are needed for the solution.

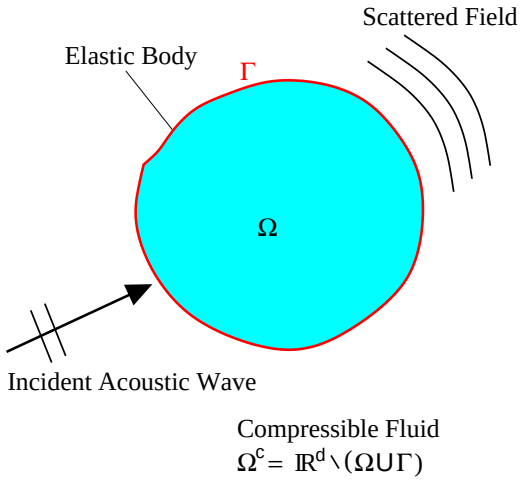

Figure 1. Acoustic wave and obstacle.

Clearly, the same numerical methods used for the inverse problems for obstacles with sound-hard and sound-soft boundaries or for penetrable obstacles can be adapted to the scattering by elastic bodies. Among the available numerical methods, in recent years sampling and factorization methods are very popular (cf. e.g. [12]). Without any a priori information about geometrical details like connectivity components or holes, these methods provide good approximations for the shape of the obstacle. The case of acoustic scattering by elastic bodies in [17] is treated by the linear sampling method. Classical methods such as in [3], [15] (cf. [4] for the case of scattering by elastic obstacles) generally require more information on the geometry of the obstacle. For instance, the boundary of the obstacle is required to be homeomorphic to a circle for 2-D and to a sphere for 3-D problems, respectively. Starting from a reasonable initial guess, the parametrization of the obstacle boundary is approximated in a Newton type iteration. Though the accuracy of the reconstructed solution is always

limited by the ill-posedness, we expect the classical Newton approach to be more accurate than the factorization methods. To avoid the solution of direct problems in each step of iteration, besides the boundaries also the wave field can be included into the components of the iterative solutions. For instance, a method proposed by Kirsch and Kress (cf. e.g. [13], [3], [25] and cf. [5] for the case of scattering by elastic obstacles) represents the waves by potentials with generating layer functions defined over artificial curves. Note that, for inverse problems in acoustic scattering by elastic obstacles, difficulties with unpleasant eigensolutions of the direct problem, referred to as Jones modes, can be avoided if the Kirsch–Kress method is applied.

In this paper we consider the two-dimensional case and compare the simple Newton method of [4] with the Kirsch–Kress method of [5] for which we present numerical results for the first time. We implement the same parametrization for the approximate boundary curves iterated by both numerical methods. For a simple egg shaped domain and for a nonconvex domain, we apply the Newton method and the Kirsch–Kress algorithm. The numerical tests show that the Kirsch–Kress method is more accurate due to the better approximation of the fields by potentials in the case of analytic boundaries. Unfortunately, this method is related to an integral equation approach for the direct problem. If the latter integral equation is severely ill-posed, then the Kirsch–Kress algorithm is divergent. Consequently, this method diverges if the curves for the potential representations are too far from the boundary curve of the true obstacle or if the latter curve has large Fourier coefficients. In particular, for the reconstruction of the nonconvex obstacle, the Kirsch–Kress method is divergent. To obtain a convergent version of this method, we use a variant with updated curves for the potential representations during the iteration. For transmission and boundary value problems in acoustic scattering, a comparable update of curves has been proposed in [24] (cf. also the curve updates in [21, Chapter 5] and [15]). Furthermore, our numerical examples reveal that the Kirsch–Kress method is more sensitive with respect to noise in the far-field data, which is also typical for a higher degree of ill-posedness. Finally, we present an example for the reconstruction of an obstacle with Jones modes. Both methods converge for this case.

We start discussing the solution of the direct problem in Section 2. Using the direct solution, we introduce the two numerical schemes for the inverse problem in Section 3. Then we recall the convergence results from [4], [5]. In Section 4 we discuss some details of the implementation. For the least squares problem of the Kirsch–Kress method, we give the formulas for the functional and its gradients in the appendix. Finally, we present the numerical results in Section 5.

2. Direct Problem: Elastic Obstacle in Fluid

Suppose a bounded elastic body is emerged in a homogeneous compressible inviscid fluid. We denote the domain of the body by Ω, its boundary

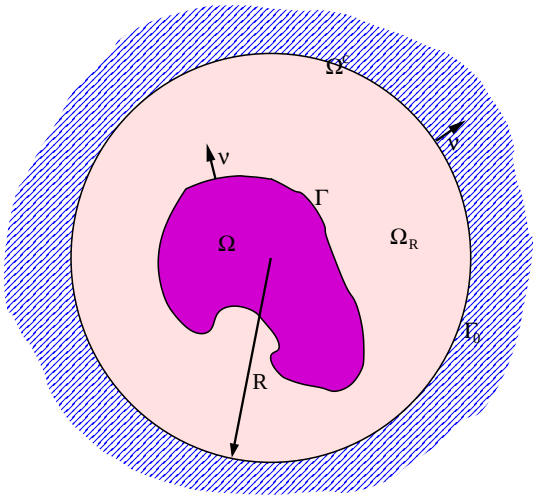

FIGURE 2. Domains.

curve by Γ (cf. Figure 2), and assume that an incoming plane wave is moving in the exterior $\Omega^c := \mathbb{R}^2 \setminus \overline{\Omega}$ toward the body. This wave is scattered by the body and generates an elastic wave inside the body. Mathematically, the acoustic wave is described by the pressure perturbation p over Ω^c and by the displacement function u on Ω. The displacement fulfills the Navier (time-harmonic Lamé) equation

$$\Delta^* u(x) + \varrho\omega^2 u(x) = 0, \quad x \in \Omega, \tag{1}$$
$$\Delta^* u(x) := \mu\Delta u(x) + (\lambda+\mu)\nabla[\nabla \cdot u(x)].$$

Here ω is the frequency, ϱ the density of body, and λ, μ are the Lamé constants. The total pressure p is the sum of the incoming wave p^{inc} and the scattered wave p^s which satisfies the Helmholtz equation and the radiation condition at infinity

$$\Delta p^s(x) + {k_w}^2 p^s(x) = 0, \quad x \in \Omega^c, \tag{2}$$
$$\frac{x}{|x|} \cdot \nabla p^s(x) - \mathbf{i}k_w p^s(x) = o(|x|^{-1/2}), \quad |x| \to \infty, \tag{3}$$

where $k_w^2 = \omega^2/c^2$ is the wave number and c the speed of sound. The pressure and the displacement field are coupled through the transmission conditions

$$u(x)\cdot\nu(x) = \frac{1}{\varrho_f\omega^2}\left\{\frac{\partial p^s(x)}{\partial\nu} + \frac{\partial p^{inc}(x)}{\partial\nu}\right\}, \quad x \in \Gamma, \tag{4}$$
$$t[u](x) = -\left\{p^s(x) + p^{inc}(x)\right\}\nu(x), \quad x \in \Gamma, \tag{5}$$
$$t[u](x) := 2\mu\,\frac{\partial u}{\partial\nu}\Big|_\Gamma + \lambda[\nabla\cdot u]\nu\big|_\Gamma + \mu\nu\times[\nabla\times u]\big|_\Gamma,$$

$$\nu \times [\nabla \times u]\big|_\Gamma := \begin{pmatrix} \nu_2(\partial_{x_1} u_2 - \partial_{x_2} u_1) \\ \nu_1(\partial_{x_2} u_1 - \partial_{x_1} u_2) \end{pmatrix} \Bigg|_\Gamma .$$

Here ϱ_f is the density of the fluid and ν denotes the unit normal at the points of Γ exterior with respect to Ω.

For numerical computations, we truncate the exterior domain Ω^c to the annular domain Ω_R with the outer boundary Γ_0 (cf. Figure 2). The Helmholtz equation (2) is solved over Ω_R, and a non-local boundary condition is imposed on Γ_0 (cf. the boundary integral equation techniques in [11]). Using standard techniques, the boundary value problem can be reformulated in a variational form and solved by the finite element method (cf. [10], [16], [4]). Suppose the boundary Γ of the obstacle is piecewise smooth and choose the auxiliary curve Γ_0 such that the corresponding interior domain has no Dirichlet eigenvalue equal to k_ω^2 for the negative Laplacian. Then existence and uniqueness of the variational solutions as well as the convergence of the finite element method (cf. [4]) can be shown whenever there is no nontrivial solution u_0 of

$$\begin{aligned} \Delta^* u_0(x) + \rho\omega^2 u_0(x) &= 0, \quad x \in \Omega, \\ t[u_0](x) &= 0, \quad x \in \Gamma, \\ u_0(x) \cdot \nu &= 0, \quad x \in \Gamma. \end{aligned} \tag{6}$$

Note that nontrivial solutions of (6) are called Jones modes, and a frequency ω, for which the given domain Ω has a nontrivial solution of (6), is called Jones frequency. It is known that domains with Jones frequencies exist but are exceptional. More precisely, Hargé [8] has shown that the set of domains with Jones frequencies is nowhere dense in a certain metric, and Natroshvili et al. [19] have proved that domains with two non-parallel flat faces have no Jones frequencies. An example of a two-dimensional domain with Jones frequency ω is the disk $\Omega_J := \{x \in \mathbb{R}^2 : \ |x| < r_J\}$ with $r_J = \frac{1}{\omega}\sqrt{\mu/\varrho}\, r_J^0$. Here r_J^0 is any of the positive roots of the equation $rJ_1'(r) = J_1(r)$, and J_1 is the Bessel function of order one. One Jones mode over Ω_J is defined by

$$u_0(x) = J_1\Big(\omega\sqrt{\frac{\varrho}{\mu}}\,|x|\Big)\begin{pmatrix} -x_2/|x| \\ x_1/|x| \end{pmatrix}, \quad x \in \Omega_J. \tag{7}$$

Note that the smallest positive root of $rJ_1'(r) = J_1(r)$ is $r_J^0 = 5.135622\ldots$. Three-dimensional Jones modes are described, e.g., in [19].

Alternatively to the finite element solution, the complete pressure function and the displacement field can be approximated by potentials with sources over auxiliary curves (cf. Figure 3). We introduce the curve Γ_i "close" to Γ, but inside Ω, and the curve Γ_e in Ω_R surrounding Γ. We represent the pressure and the displacement by

$$p^s(x) = \big[V_{\Gamma_i}^{ac}\varphi_i\big](x), \quad x \in \Omega^c, \quad u(x) = \big[V_{\Gamma_e}^{el}\vec{\varphi}_e\big](x), \quad x \in \Omega \tag{8}$$

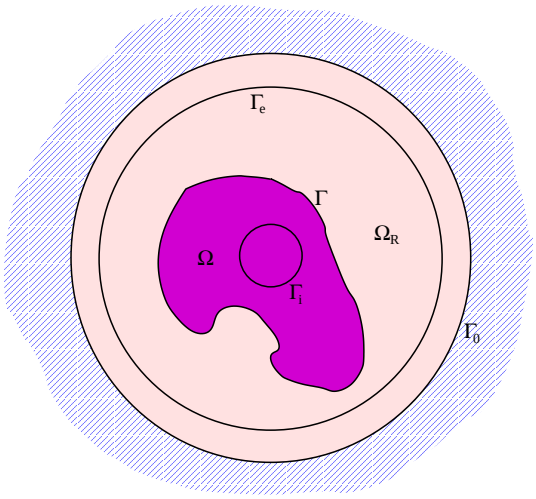

FIGURE 3. Domains and auxiliary curves

with a scalar layer function φ_i and a vector layer $\vec{\varphi}_e$. The potentials are defined by

$$\left[V_\Lambda^{ac} p\right](x) := \int_\Lambda p(y) G(x,y;k_\omega) \mathrm{d}_\Lambda y, \quad x \in \mathbb{R}^2, \tag{9}$$

$$G(x,y;k_w) := \frac{\mathbf{i}}{4} H_0^{(1)}(k_w|x-y|), \tag{10}$$

$$\left[V_\Lambda^{el} u\right](x) := \int_\Lambda G^{el}(y,x) u(y) \mathrm{d}_\Lambda y, \quad x \in \mathbb{R}^2, \tag{11}$$

$$G^{el}(y,x) := \frac{1}{\mu}\left(G(x,y;k_s)\delta_{ij} + \frac{1}{k_s^2} \frac{\partial^2 \big(G(x,y;k_s) - G(x,y;k_p)\big)}{\partial x_i \partial x_j} \right)_{i,j=1}^2,$$

where the wave numbers k_p and k_s are defined by $\varrho\omega^2 = (\lambda+2\mu)k_p^2 = \mu k_s^2$ and $H_0^{(1)}$ is the Hankel function of the first kind and of order 0. The layer functions in (8) are chosen such that the corresponding pressure and displacements fields satisfy the transmission conditions (4) and (5). In other words, to get a good approximate solution we have to solve the integral equations

$$t[V_{\Gamma_e}^{el}\vec{\varphi}_e](x) + [V_{\Gamma_i}^{ac}\varphi_i](x)\nu(x) = -p^{inc}\nu(x), \quad x \in \Gamma, \tag{12}$$

$$\varrho_f \omega^2 \nu(x) \cdot [V_{\Gamma_e}^{el}\vec{\varphi}_e](x) - \partial_\nu [V_{\Gamma_i}^{ac}\varphi_i](x) = \partial_\nu p^{inc}(x), \quad x \in \Gamma. \tag{13}$$

Numerical methods based on the discretization of (9), (11), (12) and (13) are well-known to exhibit high rates of convergence (cf. e.g. Sect. 9.8 in [6] and [2], [7], [9]). However, for not so simple geometries, an appropriate choice of Γ_i and Γ_e and an appropriate quadrature of the integrals is not

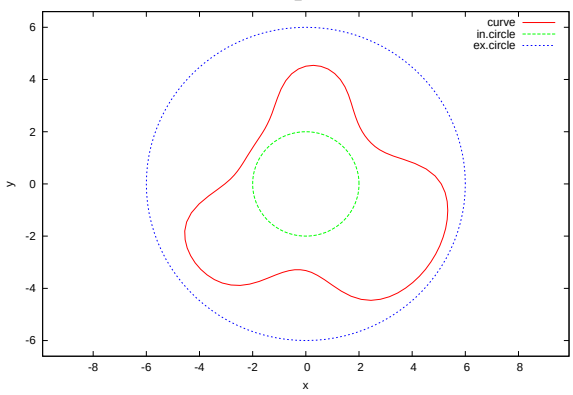

FIGURE 4. Geometry of scatterer.

trivial. A bad choice may lead to extremely ill-posed equations (12), (13) and to false results.

For a point x tending to infinity, the scattered pressure field $p^s(x)$ is known to have the following asymptotics

$$p^s(x) = \frac{e^{\mathbf{i}k_w|x|}}{|x|^{1/2}}\, p^\infty\Big(\frac{x}{|x|}\Big) + \mathcal{O}\Big(\frac{1}{|x|^{3/2}}\Big), \quad |x| \to \infty, \tag{14}$$

$$p^\infty(e^{\mathbf{i}t}) = -\frac{e^{\mathbf{i}\pi/4}}{\sqrt{8\pi k_\omega}} \int_{\Gamma_i} e^{-\mathbf{i}k_w y\cdot e^{\mathbf{i}t}}\, \varphi_i(y)\, \mathrm{d}_{\Gamma_i} y.$$

The function $\mathcal{F}[p^s](t) := p^\infty(e^{\mathbf{i}t})$ is called the far-field pattern of the scattered field. This is the entity which can be measured.

In order to prepare the numerical results for the inverse problem, we conclude this section by the computation of the corresponding direct problem. If we choose the nonconvex domain with boundary curve Γ according to Figure 4, the constants

$$\begin{aligned} &\omega = \frac{\pi}{2}\ \text{kHz}, && \varrho = 6.75\cdot 10^{-8}\ \text{kg/m}^3,\\ &\lambda = 1.287373095\ \text{Pa}, && \mu = 0.66315\ \text{Pa},\\ &c = 1500\ \text{m/s}, && \varrho_f = 2.5\cdot 10^{-8}\ \text{kg/m}^3, \end{aligned} \tag{15}$$

and the direction of the incoming plane wave equal to $v = (1,0)^\top$, then we get by the finite element method [4] the far-field pattern plotted in Figure 5.

3. Inverse Problem and Iterative Approximation

Now we suppose that the boundary curve Γ of the obstacle is star-shaped and included between the inner curve $\Gamma_i := \{x \in \mathbb{R}^2 : \ |x| = r_i\}$ and the

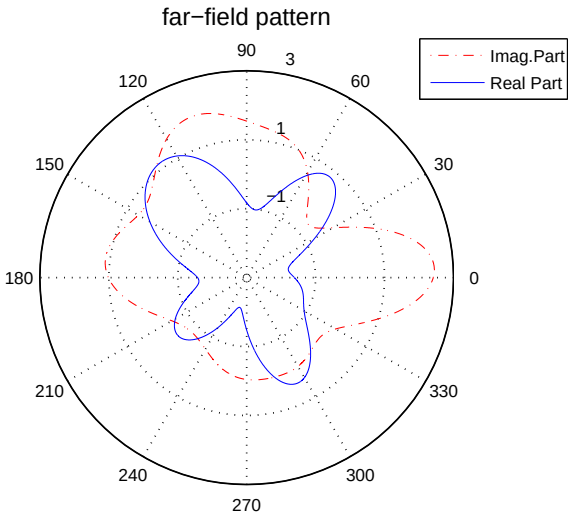

FIGURE 5. Far-field pattern.

outer curve $\Gamma_e := \{x \in \mathbb{R}^2 : \ |x| = r_e\}$, i.e.,

$$\Gamma := \left\{\mathbf{r}(t)e^{\mathbf{i}t} : \ 0 \le t \le 2\pi\right\}, \quad \mathbf{r}(t) = \widehat{a}_0 + \sum_{j=1}^{\infty} \left\{\widehat{a}_j \cos(jt) + \widehat{b}_j \sin(jt)\right\} \quad (16)$$

with the constraint $r_i < \mathbf{r}(t) < r_e$, $0 \le t \le 2\pi$. To avoid this constraint, we can use the parametrization $\Gamma = \Gamma^{\mathbf{r}}$

$$\Gamma^{\mathbf{r}} := \left\{\widetilde{\mathbf{r}}(t)e^{\mathbf{i}t} : \ 0 \le t \le 2\pi\right\}, \quad \widetilde{\mathbf{r}}(t) := \frac{r_e + r_i}{2} + \frac{r_e - r_i}{\pi} \arctan(\mathbf{r}(t)). \quad (17)$$

Having in mind this representation, the star-shaped curve is uniquely determined by the real valued function $\mathbf{r}$ or, equivalently, by the Fourier coefficients $\{\widehat{a}_j, \widehat{b}_j\}$. The direct problem of the previous section defines a continuous mapping (cf. [4])

$$F : H^{1+\varepsilon}_{per}[0, 2\pi] \longrightarrow L^2_{per}[0, 2\pi], \quad \mathbf{r} \mapsto p^{\infty},$$

where $p^{\infty} = \mathcal{F}[p^s]$ is the far-field of the scattered field p^s, and p^s is the pressure part of the solution (p^s, u) to the direct problem (1), (2), (4), (5), and (3) including the interface $\Gamma = \Gamma^{\mathbf{r}}$ and a fixed incoming plane wave p^{inc}. The space $H^{1+\varepsilon}_{per}[0, 2\pi]$ is the periodic Sobolev space of order $1 + \varepsilon > 1$ over the interval $[0, 2\pi]$. $L^2[0, 2\pi]$ is the corresponding Lebesgue space. Now the inverse problem is the following: For a given far-field pattern p^{∞}, find the shape of the obstacle with boundary $\mathbf{r}_{sol}$ such that the scattered field corresponding to the fixed incoming plane wave p^{inc} has the far-field pattern p^{∞}, i.e., such that $F(\mathbf{r}_{sol}) = p^{\infty}$. To our knowledge, results on the uniqueness of the solution $\mathbf{r}_{sol}$ are not known yet. For the case of far-field

data given in all directions of incidence, we refer to the theoretical results in [18], [17].

We now define three different optimization problems equivalent to the inverse problem. Numerical algorithms for the inverse problem can be derived simply by applying numerical minimization schemes to the optimization problems. More precisely, the minimization schemes are applied to regularized modifications of the optimization problems.

The first optimization problem is to find a least-squares solution $\mathbf{r}_{min}$, i.e., a minimizer of the following problem

$$\inf_{\mathbf{r}\in H^{1+\varepsilon}_{per}[0,2\pi]} \mathcal{J}_\gamma(\mathbf{r}), \quad \mathcal{J}_\gamma(\mathbf{r}) := \left\| F(\mathbf{r}) - p^\infty \right\|^2_{L^2[0,2\pi]}.$$

Since the inverse problem is ill-posed and since the measured far-field data is given with noise, we replace the last optimization problem by

$$\inf_{\mathbf{r}\in H^{1+\varepsilon}_{per}[0,2\pi]} \mathcal{J}^1_\gamma(\mathbf{r}), \quad \mathcal{J}^1_\gamma(\mathbf{r}) := \left\| F(\mathbf{r}) - p^\infty_{noisy} \right\|^2_{L^2[0,2\pi]} + \gamma \|\mathbf{r}\|^2_{H^{1+\varepsilon}_{per}[0,2\pi]}, \quad (18)$$

where γ is a small positive regularization parameter. As usual this parameter is to be chosen in dependence on the noise level. To guarantee convergence for noise level tending to zero and for $\gamma \to 0$, we suppose

$$\left\| p^\infty - p^\infty_{noisy} \right\|^2_{L^2[0,2\pi]} \le c\gamma \quad (19)$$

for a constant c independent of γ. The first numerical algorithm (cf. [4]) consists now in discretizing the mapping F by finite elements and applying a Gauss–Newton method to determine a minimizer of (18). This is a modified Newton method for the operator equation $F(\mathbf{r}_{sol}) = p^\infty_{noisy}$ which we shall call the simple Newton iteration.

Theorem 3.1 ([4]). *Suppose Γ_0 is chosen such that the corresponding interior domain has no Dirichlet eigenvalue equal to k^2_ω for the negative Laplacian. Then we have:*

(i) *For any $\gamma > 0$, there is a minimizer $\mathbf{r}^\gamma$ of* (18).

(ii) *Suppose the far-field pattern p^∞ is the exact pattern for a fixed solution $\mathbf{r}^*$ of the inverse problem, i.e., $F(\mathbf{r}^*) = p^\infty$ and $\mathcal{J}^1_0(\mathbf{r}^*) = 0$. Then, for $\varepsilon > 0$ and for any set of minimizers $\mathbf{r}^\gamma$, there exists a subsequence $\mathbf{r}^{\gamma_n}$ converging weakly in $H^{1+\varepsilon}_{per}[0,2\pi]$ and strongly in $H^{1+\varepsilon'}_{per}[0,2\pi]$, $0 < \varepsilon' < \varepsilon$, to a solution $\mathbf{r}^{**}$ of* (18) *with $\gamma = 0$ and, therewith, to a solution of the inverse problem.*

(iii) *If, additionally to the assumptions of* (iii), *the solution $\mathbf{r}^*$ of the inverse problem is unique, then we even get that $\mathbf{r}^\gamma$ tends to $\mathbf{r}^*$ weakly in $H^{1+\varepsilon}_{per}[0,2\pi]$ and strongly in $H^{1+\varepsilon'}_{per}[0,2\pi]$, $0 < \varepsilon' < \varepsilon$.*

Unfortunately, for the first method the computation of F requires a solution of a direct problem. In particular, if the curve Γ is the boundary of a domain with Jones frequency or close to such a boundary, the direct solution by finite elements is not easy. One way would be to compute with slightly modified frequencies. However, it might be difficult to check whether the

curve is "close" to the boundary of a domain with Jones frequency and to choose a modified frequency appropriately.

In order to motivate the second numerical method, the Kirsch–Kress algorithm, which corresponds to a third optimization problem, we introduce a second intermediate optimization method first. The plan is to define a method, where a solution of the direct method is not needed. Therefore, besides the unknown curve Γ the pressure p^s and the displacement field u are included into the set of optimization "parameters". Additionally to the term of the least squares deviation of $\mathcal{F}[p^s]$ from p^∞_{noisy}, new terms are needed which enforce the fulfillment of the equations (1), (2), (4), (5), and (3) at least approximately. Hence, the regularized second optimization problem is to find a minimizer $(\mathbf{r}_{min}, u_{min}, p_{min})$ of

$$\inf_{\mathbf{r}\in H^{2+\varepsilon}_{per}[0,2\pi],\ u\in[H^1(\Omega)]^2,\ p^s\in H^1(\Omega_R)} \mathcal{J}^2_\gamma(\mathbf{r},u,p^s), \tag{20}$$

$$\begin{aligned}
\mathcal{J}^2_\gamma(\mathbf{r},u,p^s) := {} & \left\|\mathcal{F}[p^s]-p^\infty_{noisy}\right\|^2_{L^2[0,2\pi])} + \left\|\Delta^* u+\varrho\omega^2 u\right\|^2_{[H^{-1}(\Omega)]^2}+\\
& + \left\|\Delta p^s + {k_w}^2 p^s\right\|^2_{H^{-1}(\Omega_R)}+\\
& + \left\|t[u]+\{p^s+p^{inc}\}\nu\right\|^2_{[H^{-1/2}(\Gamma)]^2}+\\
& + \left\|u\cdot\nu-\frac{1}{\varrho_f\omega^2}\left\{\frac{\partial p^s}{\partial\nu}+\frac{\partial p^{inc}}{\partial\nu}\right\}\right\|^2_{H^{-1/2}(\Gamma)}+\\
& + \left\|V^{ac}_{\Gamma_0}[\partial_\nu p^s]+\frac{1}{2}[p^s]-K^{ac}_{\Gamma_0}[p^s]\right\|^2_{H^{1/2}(\Gamma_0)}+\\
& + c_1\gamma\|\mathbf{r}\|^2_{H^{2+\varepsilon}_{per}[0,2\pi]} + c_2\gamma\|u\|^2_{H^1(\Omega)} + c_3\gamma\|p^s\|^2_{H^1(\Omega_R)},\\
K^{ac}_{\Gamma_0}[p^s](x) := {} & \int_{\Gamma_0}\frac{\partial G(x,y;k_w)}{\partial\nu(y)}\,p^s(y)\,\mathrm{d}_{\Gamma_0}y
\end{aligned}$$

where $c_i > 0$, $i = 1,2,3$, are calibration constants and γ is a small positive regularization parameter. Of course, this is a theoretical optimization problem only. For a numerical realization, the operators should be replaced by those of the variational formulation. However, it is clearly seen that the price for avoiding a solution of the direct problem is an increase in the number of the optimization "parameters". The numerical solution of the discretized optimization problem (20) is higher dimensional and might be more involved than that for the case of (18).

The third optimization problem is a modification of (20). The optimization "parameters" u and p^s are replaced by the layer functions φ_i and $\vec{\varphi}_e$ of the potential representations (8). In other words, in the numerical discretization the finite elements over the domains Ω and Ω_R are replaced by lower dimensional boundary elements over the curves Γ_i and Γ_e. Instead of the terms in $\mathcal{J}^2_\gamma$ enforcing the conditions (1), (2), (4), (5), and (3), we only

need terms enforcing (12) and (13). Hence, the regularized third optimization problem is to find a minimizer $(\mathbf{r}_{min}, \varphi_{i,min}, \vec{\varphi}_{e,min})$ of

$$\inf_{\mathbf{r}\in H^{2+\varepsilon}_{per}[0,2\pi],\ \varphi_i\in H^{-1}(\Gamma_i),\ \vec{\varphi}_e\in[H^{-1}(\Gamma_e)]^2} \mathcal{J}^3_\gamma(\mathbf{r},\varphi_i,\vec{\varphi}_e), \tag{21}$$

$$\begin{aligned}\mathcal{J}^3_\gamma(\mathbf{r},\varphi_i,\vec{\varphi}_e) := c\Big\|\mathcal{F}\big[V^{ac}_{\Gamma_i}\varphi_i\big] - p^\infty_{noisy}\Big\|^2_{L^2[0,2\pi]} + \\ + \gamma\|\varphi_i\|^2_{H^{-1}(\Gamma_i)} + \gamma\|\vec{\varphi}_e\|^2_{[H^{-1}(\Gamma_e)]^2} + \\ + \Big\|t\big[V^{el}_{\Gamma_e}\vec{\varphi}_e\big] + \big[V^{ac}_{\Gamma_i}\varphi_i\big]\nu + p^{inc}\nu\Big\|^2_{L^2(\Gamma^{\mathbf{r}})} + \\ + \Big\|\varrho_f\omega^2\nu\cdot\big[V^{el}_{\Gamma_i}\vec{\varphi}_e\big] - \partial_\nu\big[V^{ac}_{\Gamma_i}\varphi_i\big] - \partial_\nu p^{inc}\Big\|^2_{L^2(\Gamma^{\mathbf{r}})},\end{aligned} \tag{22}$$

where γ is a small positive regularization parameter and c a positive calibration constant. We choose the layers $\varphi_{i,min}$ and $\vec{\varphi}_{e,min}$ in an unusual Sobolev space of negative order to enable approximations by Dirac-delta functionals, i.e., by the method of fundamental solutions. Though the number of optimization parameters in a discretization of (21) is larger than that in a discretization of (18), the objective functional $\mathcal{J}^3_\gamma$ is simpler than $\mathcal{J}^1_\gamma$. Applying an optimization scheme like the conjugate gradient method or the Levenberg–Marquardt algorithm to (21), we arrive at the Kirsch–Kress method. Note that the accuracy of the solution of this method is limited by the accuracy of solving the integral equations (12) and (13) with a Tikhonov regularization. To improve this, the curves Γ_i and Γ_e can be updated during the iterative solution of the optimization problem (compare the iterative schemes in [21], [24], [15]).

Theorem 3.2 ([5]). *Suppose k^2_ω is not a Dirichlet eigenvalue for the negative Laplacian in the interior of Γ_i and that p^∞ is the exact far-field pattern of a scattered field p^s corresponding to some $\Gamma^{\mathbf{r}^*}$. Then we have:*

(i) *For any $\gamma > 0$, there is a minimizer $(\mathbf{r}^\gamma, \varphi^\gamma_i, \vec{\varphi}^\gamma_e)$ of (21).*

(ii) *For any set of minimizers $(\mathbf{r}^\gamma, \varphi^\gamma_i, \vec{\varphi}^\gamma_e)$, there exists a subsequence $(\mathbf{r}^{\gamma_n}, \varphi^{\gamma_n}_i, \vec{\varphi}^{\gamma_n}_e)$ such that $\mathbf{r}^{\gamma_n}$ converges weakly in $H^{1+\varepsilon}_{per}[0,2\pi]$ and strongly in $H^{1+\varepsilon'}_{per}[0,2\pi]$, $0<\varepsilon'<\varepsilon$, to a solution $\mathbf{r}^{**}$ of the inverse problem.*

(iii) *If, additionally, the solution $\mathbf{r}^*$ of the inverse problem is unique, then we even get that $\mathbf{r}^\gamma$ tends to $\mathbf{r}^*$ weakly in $H^{1+\varepsilon}_{per}[0,2\pi]$ and strongly in $H^{1+\varepsilon'}_{per}[0,2\pi]$, $0<\varepsilon'<\varepsilon$.*

Formulas for the discretization of the optimization problem (21) and for the derivatives of the objective functional are presented in Section 6.

4. Some Details of the Implementation

For the solution of the optimization problems, a lot of **numerical optimization schemes** are available (cf. [20]). Unfortunately, global methods

which yield the global minimum are often very slow. We recommend gradient based local optimization schemes. They provide local minimizers, i.e. solutions with minimal value of the objective functional in a neighbourhood of the minimizer. In general, it cannot be guaranteed that the local minimizer is the global minimizer. However, using a good initial guess, the local minimizer will coincide with the global. In particular, we have tested the Gauss–Newton method, the Levenberg–Marquardt algorithm (cf. [14]), and the conjugate gradient method. The last method has been tested for the Kirsch–Kress method to avoid the solution of linear systems in the size of the direct problem.

In order to compute **derivatives** of the objective functionals in case of the simple Newton iteration the calculus of shape derivatives can be applied. The derivatives result from solving the finite element system of the direct problem with new right-hand side vectors. This is fast if the finite element system is solved by an LU factorization for sparse systems (cf. [22], [4]). The derivatives for the Kirsch–Kress method can be obtained by a simple differentiation of the kernel functions in the potential representations. Since the elasticity kernel contains second-order derivatives of the acoustic kernel and since the terms enforcing the transmission conditions contain first-order derivatives of the elastic potential, we need fourth order derivatives of the acoustic kernel. We present the needed formulas in Section 6.

Normally, **quadrature** rules are needed if the layer functions φ_i and $\vec{\varphi}_e$ in the potential representation (8) are approximated by functions of a finite dimensional space. The potential integrals of these functions must be approximated by appropriate quadratures. However, in the case of the Kirsch–Kress method we can approximate the layer functions by linear combinations of Dirac delta functions

$$\varphi_i \sim \varphi_{i,M} := \sum_{\kappa=1}^{M} b_\kappa \delta_{x_{i,\kappa}}, \quad b_\kappa \in \mathbb{C}, \quad x_{i,\kappa} := r_i e^{\mathbf{i}t_\kappa}, \quad t_\kappa := \frac{2\pi\kappa}{M}, \tag{23}$$

$$\vec{\varphi}_e \sim \vec{\varphi}_{e,M} := \sum_{\kappa=1}^{M} c_\kappa \delta_{x_{e,\kappa}}, \quad c_\kappa \in \mathbb{C}^2, \quad x_{e,\kappa} := r_e e^{\mathbf{i}t_\kappa}. \tag{24}$$

This works since the potential operators are smoothing operators from the curve Γ_e, Γ_i to Γ. Only in the case that Γ_e or Γ_i is close to Γ, a trigonometric or spline approximation of φ_i and $\vec{\varphi}_e$ together with an accurate quadrature must be employed.

Another important issue is the **scaling** of the optimization scheme. Indeed, the number of necessary iterations depends on the conditioning of the optimization problem. Using an appropriate scaling, the conditioning can be essentially improved. The first choice is, of course, the natural scaling. The far-field values should be scaled such that the measurement uncertainties of the scaled far-field values coincide, and the parameters should be scaled in accordance with the accuracy requirements. A scaling different from the natural one is chosen not to improve the reconstruction operator,

but to speed up the optimization algorithm. This calibration may include different constants in front of the individual terms in the objective functional (cf. the factors c and γ in the definition of $\mathcal{J}_\gamma^3$) and the replacement of the optimization parameters by the products of these parameters with convenient constants. The constants can be chosen, e.g., to minimize the conditioning of the Jacobian of the mapping that maps the parameters to the far-field values. Alternatively, the constants can be chosen by checking typical test examples with known solution. To improve the conditioning of the optimization in the Kirsch–Kress method, we have replaced the "optimization parameters" $\mathbf{r}$, φ_i, and $\vec{\varphi}_e$ by the parameters

$$\mathbf{r}' = \mathbf{r}/c_{\mathbf{r}}, \quad \varphi_i' = \varphi_i/c_i, \quad \vec{\varphi}_e' = \vec{\varphi}_e/c_e. \tag{25}$$

5. Numerical Results

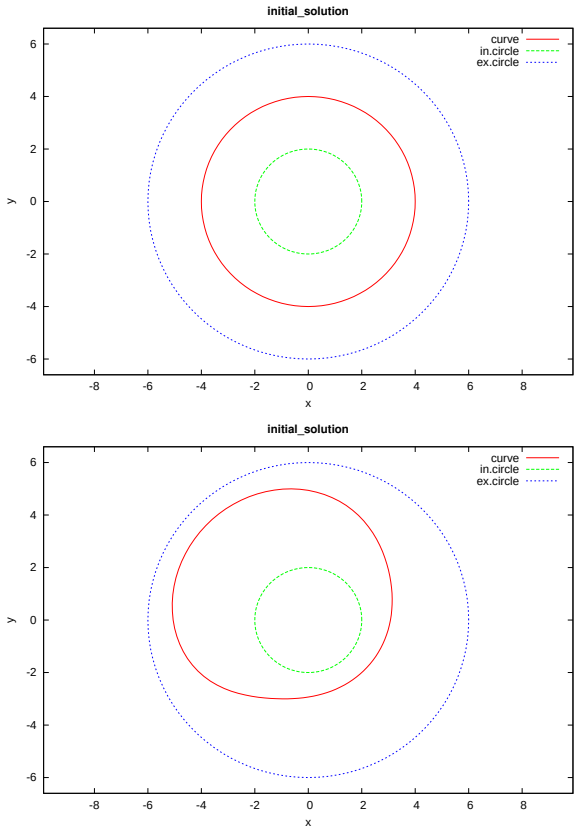

Figure 6. Initial solution and egg shaped domain.

5.1. **The curves for the numerical examples and some technical details.** We have employed (i) the simple Newton iteration and (ii) the

Kirsch–Kress method, both with a circle as initial solution, to reconstruct two different obstacles. The first is an easy egg shaped domain (cf. Figure 6) with a boundary given by (17), by $r_i = 2$, $r_e = 6$, and by the fast decaying Fourier coefficients

$$\begin{array}{llllllllll} \widehat{a}_0 = & 0, & & & & & & & & \\ \widehat{a}_1 = -1, & \widehat{a}_2 = & 0.1, & \widehat{a}_3 = & 0.01, & \widehat{a}_4 = & -0.001, & \widehat{a}_5 = 0.0001, \\ \widehat{b}_1 = & 1, & \widehat{b}_2 = & 0.1, & \widehat{b}_3 = & 0.01, & \widehat{b}_4 = & 0.001, & \widehat{b}_5 = 0.0001. \end{array} \tag{26}$$

The second body is the nonconvex obstacle from the end of Section 2 (cf. Figure 7), and its boundary is given by $r_i = 2$, $r_e = 6$ and by the Fourier coefficients

$$\begin{array}{llllllllll} \widehat{a}_0 = & 0, & & & & & & & & \\ \widehat{a}_1 = & 1, & \widehat{a}_2 = & 0.10, & \widehat{a}_3 = & 0.040, & \widehat{a}_4 = & 0.016, & \widehat{a}_5 = & 0.008, \\ \widehat{b}_1 = -1, & \widehat{b}_2 = & 0.02, & \widehat{b}_3 = & -1.500, & \widehat{b}_4 = & -0.010, & \widehat{b}_5 = & 0.008. \end{array} \tag{27}$$

Clearly, both obstacles are defined by a truncated Fourier series and are analytic. However, the egg shaped domain is smoother since the nonzero Fourier coefficients have the strong decay property $|\widehat{a}_j| \le 10^{-j}$ and $|\widehat{b}_j| \le 10^{-j}$. More precisely, the norms

$$\|\mathbf{r}\|_r := \sqrt{|\widehat{a}_0|^2 + \frac{1}{2}\sum_{j=1}^{\infty} r^{-2j}|\widehat{a}_j|^2 + \frac{1}{2}\sum_{j=1}^{\infty} r^{-2j}|\widehat{b}_j|^2}\,, \quad r > 1,$$

of analytic functions are smaller for the egg shaped domain than for the nonconvex example. Note that $\|\mathbf{r}\|_r$ is the norm

$$\sqrt{|\widehat{a}_0|^2 + \sum_{j=1}^{\infty} r^{-2j}\Big|\frac{\widehat{a}_j - \mathbf{i}\widehat{b}_j}{2}\Big|^2 + \sum_{j=1}^{\infty} r^{-2j}\Big|\frac{\widehat{a}_j + \mathbf{i}\widehat{b}_j}{2}\Big|^2},$$

of the analytic extension

$$z = \varrho e^{\mathbf{i}t} \mapsto \widehat{a}_0 + \sum_{j=1}^{\infty}\Big[\frac{\widehat{a}_j - \mathbf{i}\widehat{b}_j}{2}\Big]\varrho^j e^{\mathbf{i}jt} + \sum_{j=1}^{\infty}\Big[\frac{\widehat{a}_j + \mathbf{i}\widehat{b}_j}{2}\Big]\varrho^{-j} e^{-\mathbf{i}jt}$$

of the function $e^{\mathbf{i}t} \mapsto \mathbf{r}(t) = \sum_j \widehat{a}_j \cos(jt) + \sum_j \widehat{b}_j \sin(jt)$ onto the annular domain $\{z \in \mathbb{C} :\ 1/r < |z| < r\}$.

In all computations, we have chosen the physical constants in accordance with (15). The incoming plane wave has been fixed to $p^{inc}(x) := e^{\mathbf{i}(1,0)^\top \cdot x}$. Moreover, for all initial curves and all iterative solutions, we have fixed the zeroth Fourier coefficient $\widehat{a}_0$ to zero. The "measured" far-field data $\{p^\infty(k/M''), k = 1, \ldots, M''\}$, $M'' = 80$ (cf. Figure 5) has been simulated by the piecewise linear finite element method (FEM) described in Section 2. To avoid what is called an inverse crime, we have chosen the meshsize of the FEM grid (determined by NETGEN [23]) for the far-field computation by a factor of at least 0.25 smaller than that of the FEM grids involved in the

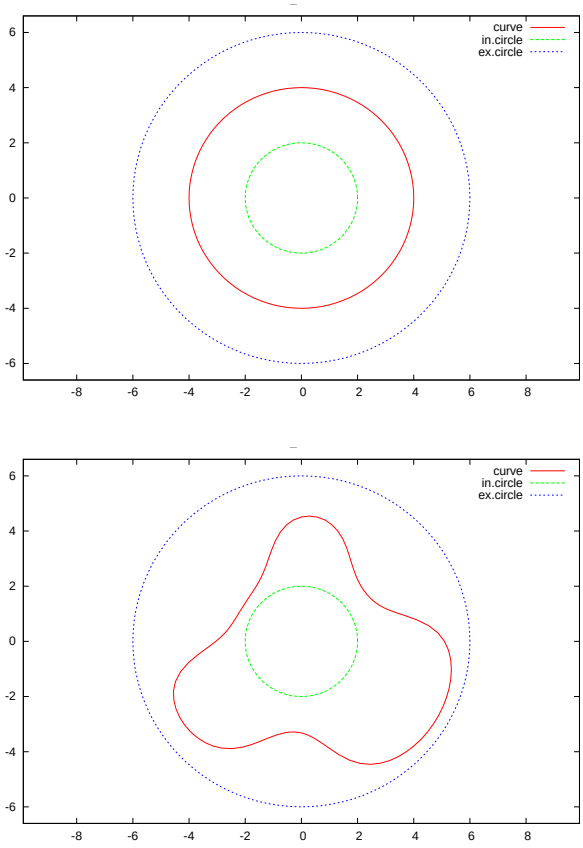

FIGURE 7. Initial solution and nonconvex domain.

inverse algorithms. Our tests have revealed that the far-field of the FEM method is more reliable than that computed by the regularized system (12)–(13). The scaling parameters c, $c_{\mathbf{r}}$, c_i, and c_e for the Kirsch–Kress method (cf. (25) and the definition of $\mathcal{J}_\gamma^3$) have been determined experimentally such that the reconstruction by Gauss–Newton iteration converges with the smallest number of iteration steps. For example, for the egg shaped domain and $M = M' = 44$ points of discretization for the approximate integration over Γ, Γ_i, Γ_e (cf. the discretized objective functional in (A.6)), these values are $c = 4000$, $c_{\mathbf{r}} = 1$, $c_i = 0.1$, and $c_e = 0.005$.

5.2. **Convergence of the simple Newton iteration.** The results for the egg shaped domain and for the simple Newton iteration have been similar to those presented in [4], where the constants where slightly different and the obstacle was similar to our nonconvex body. After a small number (≤ 20) of iterations, the algorithm reconstructs the obstacle. The regularization parameter γ can even be set to zero, which is not surprising since only

10 unknown real parameters are reconstructed from 160 real measurement values. The left Table 1 exhibits the meshsize h, the number of Gauss–Newton iterations it, and the accuracy $err := \|\widetilde{\mathbf{r}} - \widetilde{\mathbf{r}}_{FEM}\|_{L^\infty[0,2\pi]}$ of the reconstruction $\mathbf{r}_{FEM}$. The first row contains the accuracy of the initial guess. For the nonconvex obstacle, the results are similar (cf. right Table 1). Most of the computing time is spent on the evaluation of the objective functional including the solution of a direct problem. Therefore, it is not necessary to replace the expensive Gauss–Newton iteration by a different optimization scheme.

h	err	it
	1.2596	0
0.5	0.0759	6
0.25	0.0247	8
0.125	0.00876	8
0.0625	0.00329	10
0.03125	0.00156	10

h	err	it
	1.5733	0
0.25	1.1435	20
0.125	0.00924	17
0.0625	0.00401	15
0.03125	0.00157	18

TABLE 1. Reconstruction by simple Newton iteration for egg shaped domain (left) and for nonconvex domain (right).

5.3. **Convergence of the Kirsch–Kress algorithm.** We have started the tests of the Kirsch–Kress method with the nonconvex domain. However, the optimization algorithms did not converge. To fix the problem, we have checked the solution of the corresponding direct problem. We have observed that the far-field of the solution computed by (8), (12), and (13) did not match that of the FEM. Even a Tikhonov regularization in accordance with the last four terms of the functional $\mathcal{J}_\gamma^3$ did not help. Only a regularization with a truncated singular value decomposition and a well-chosen truncation parameter led to the correct far field. In other words, the reason for the divergence of the Kirsch–Kress method is the high degree of ill-posedness of the system (12), (13). On the other hand, if we commit the inverse crime and take the incorrect far-field data computed by solving (12), (13), then the Kirsch–Kress algorithm does converge.

To show the convergence of the Kirsch–Kress method with FEM generated far-field data, we consider the egg shaped domain. This time the solution curve has a higher degree of smoothness, and the direct solution of (12), (13) together with a Tikhonov regularization yields a far-field solution close to that of the FEM. Table 2 shows that the Kirsch–Kress method converges for the egg shaped domain. Indeed, the table shows the regularization parameter γ, the error $\|\widetilde{\mathbf{r}} - \widetilde{\mathbf{r}}_{KK}\|_{L^\infty_{per}[0,2\pi]}$ of the Kirsch–Kress reconstruction $\mathbf{r}_{KK}$, and the number of necessary iteration steps. These depend on the number of discretization points $M = M'$ for the approximate integration over Γ, Γ_i, Γ_e (cf. the discretized objective functional in

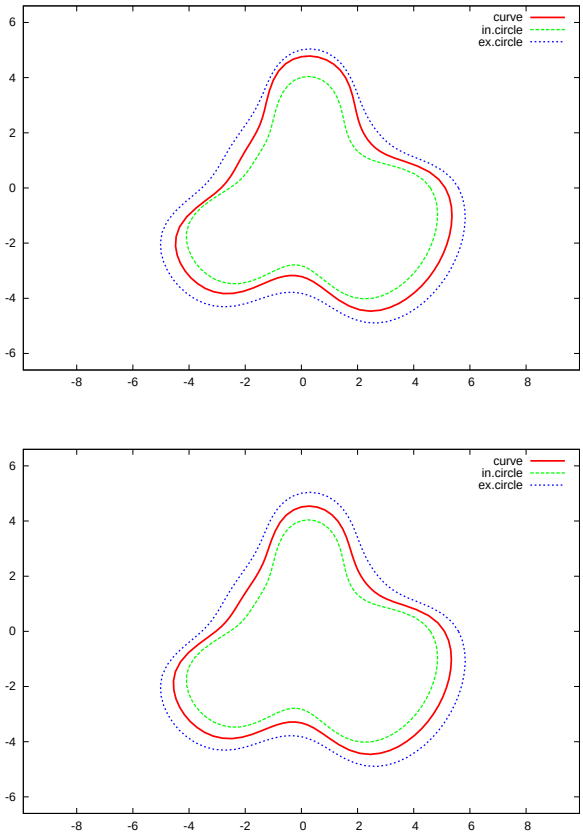

FIGURE 8. Initial solution with Fourier coefficients $\widehat{a}_i^1, \widehat{b}_i^1$ and nonconvex domain with modified curves Γ_i and Γ_e.

(A.6)) and on the choice of the optimization method. In particular, we have checked the Gauss–Newton method with experimentally chosen regularization parameter γ (GNw), the Levenberg–Marquardt method with the same regularization parameter (LMw), and the Levenberg–Marquardt method without regularization (LMo). The results show much better approximations than for the simple Newton iteration. Unfortunately, the conjugate gradient method did not converge.

To get convergence of the Kirsch–Kress method also for the nonconvex domain of Figure 7, we have changed the curves Γ_i and Γ_e (cf. Figure 8). If these are closer to the curve $\Gamma^{\mathbf{r}}$, then the degree of ill-posedness of the operators in (12), (13) is reduced. We have chosen the initial guess of the Fourier coefficients as

$$\begin{array}{lllll} \widehat{a}_0^0 = 0.0, & & & & \\ \widehat{a}_1^0 = 1.3, & \widehat{a}_2^0 = -0.10, & \widehat{a}_3^0 = 0.1, & \widehat{a}_4^0 = -0.05, & \widehat{a}_5^0 = 0.018, \\ \widehat{b}_1^0 = -0.8, & \widehat{b}_2^0 = 0.05, & \widehat{b}_3^0 = -1.7, & \widehat{b}_4^0 = 0.03, & \widehat{b}_5^0 = -0.020. \end{array} \tag{28}$$

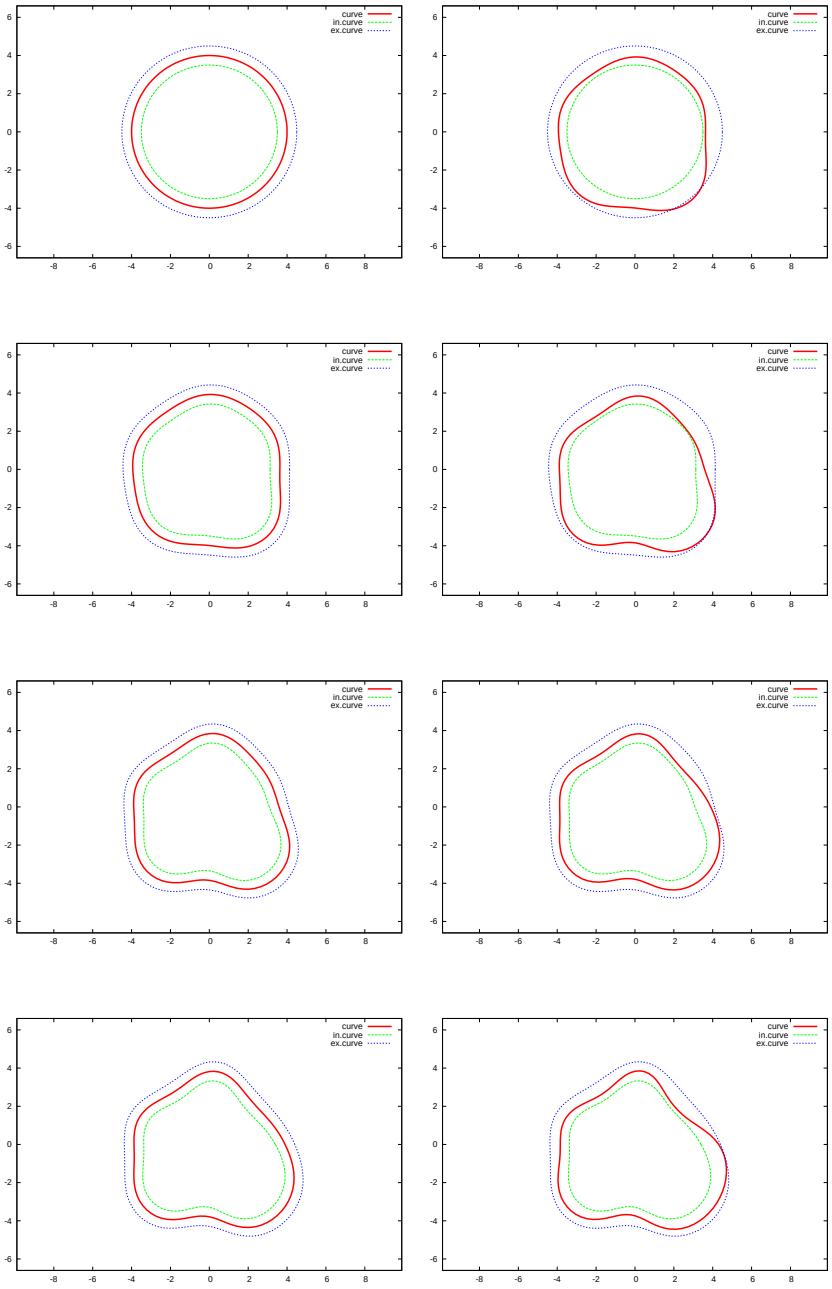

FIGURE 9. Kirsch–Kress steps 1-4 to reconstruct nonconvex domain.

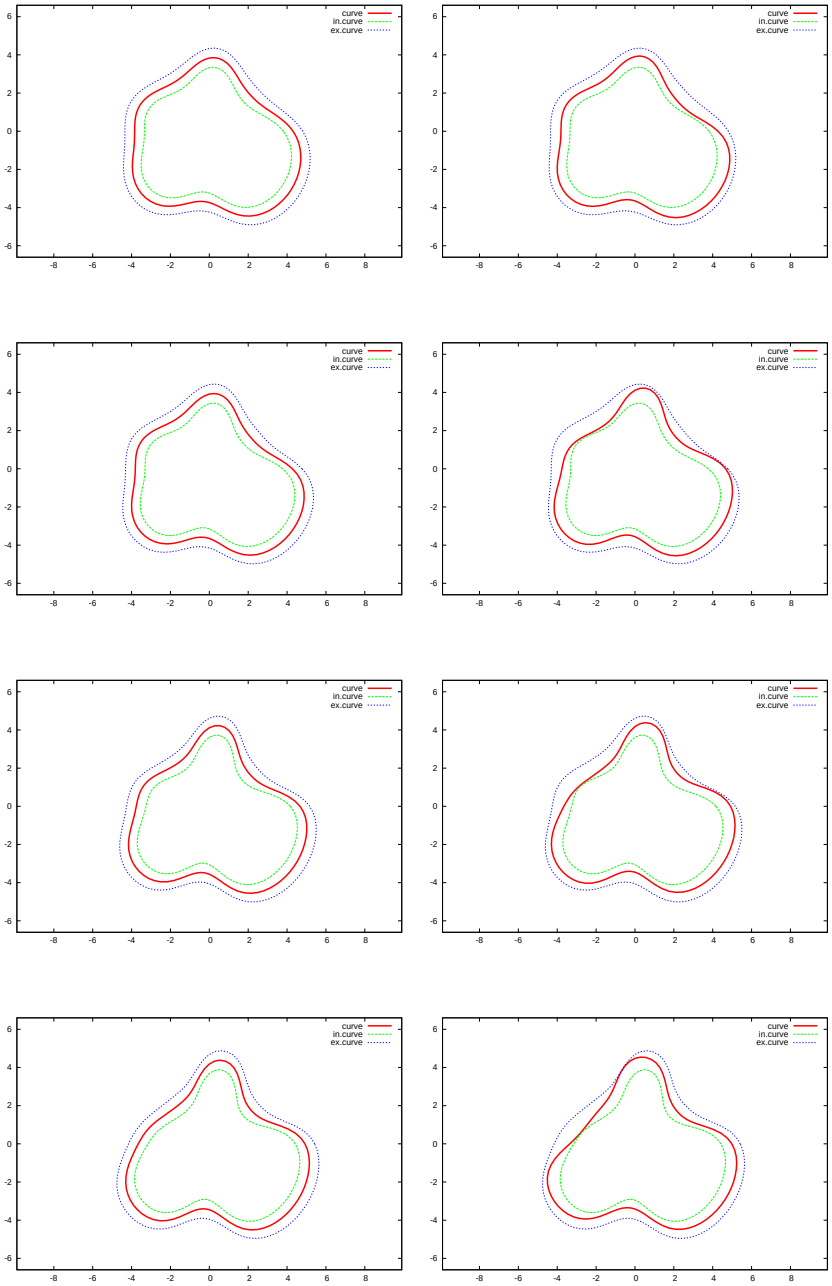

FIGURE 10. Kirsch–Kress steps 5-8 to reconstruct nonconvex domain.

number of pnts. $M = M'$	γ	GNw		LMw		LMo	
		1.2596	(0)	1.2596	(0)	1.2596	(0)
22	$4 \cdot 10^{-8}$	0.05427	(13)	0.05461	(30)	0.06793	(30)
44	$0.25 \cdot 10^{-12}$	0.002136	(13)	0.002007	(320)	0.002095	(320)
88	$4 \cdot 10^{-14}$	0.0002126	(13)	0.0002107	(80)	0.0001997	(160)

TABLE 2. Reconstruction accuracy (number of iterations) in dependence on the optimization method and on the number of discretization points for the egg shaped domain.

Since the iteration, with this initial solution, converged to a false local minimum, we have introduced an initial solution closer to the true solution in (27). We have checked the initial solution

$$\widehat{a}_i^1 := \frac{1}{2}\big(\widehat{a}_i^0 + \widehat{a}_i\big), \quad i = 0, \dots, 5, \quad \widehat{b}_i^1 := \frac{1}{2}\big(\widehat{b}_i^0 + \widehat{b}_i\big), \quad i = 1, \dots, 5$$

and observed convergence. In particular, we had to choose a larger number of discretization points on the curves Γ, Γ_i, Γ_e, namely $M = M' = 352$. We have set the regularization parameter $\gamma = 10^{-8}$ and the scaling constants to $c = 10000$, $c_{\mathbf{r}} = 1$, $c_i = 1$, and $c_e = 0.2$. For the initial solution $\{\widehat{a}_i^1, \widehat{b}_i^1\}$, we got the reconstructed curve within 11 iterations of the Gauss-Newton method. The error $\|\widetilde{\mathbf{r}} - \widetilde{\mathbf{r}}_{ini}\|_{L^\infty[0,2\pi]} = 0.296$ of the initial parametrization $\mathbf{r}_{ini}$ with Fourier coefficients $\widehat{a}_i^1, \widehat{b}_i^1$ has been reduced to $\|\widetilde{\mathbf{r}} - \widetilde{\mathbf{r}}_{KK}\|_{L^\infty[0,2\pi]} = 0.000279$.

5.4. **Kirsch–Kress algorithm with updated representation curves.** Now we suppose that, for the reconstruction of the nonconvex domain, we have an initial solution like the disk on the left in Figure 7. In order to have the curves Γ_i and Γ_e close to the iterate $\Gamma^{\mathbf{r}_n}$, we have to update Γ_i and Γ_e during the iteration process. More precisely, in each step of the iteration, we proceed as follows:

- We choose $\Gamma_i = \Gamma^{\mathbf{r}_i}$ and $\Gamma_e = \Gamma^{\mathbf{r}_e}$ with $\mathbf{r}_i = \mathbf{r}_{n-1} - 0.5$ and $\mathbf{r}_e = \mathbf{r}_{n-1} + 0.5$ (cf. (17)). Thus Γ_i and Γ_e deviate from the curve $\Gamma^{\mathbf{r}_{n-1}}$ of the previous step by the same amount as the fixed curves Γ_i and Γ_e from the true solution $\Gamma^{\mathbf{r}}$ on the right in Figure 8.
- With these Γ_i and Γ_e we perform a single step of the Gauss-Newton iteration and get the new solution $\Gamma^{\mathbf{r}'_n}$.
- If the resulting $\Gamma^{\mathbf{r}'_n}$ is enclosed between Γ_i and Γ_e, then we choose the new iterate $\mathbf{r}_n = \mathbf{r}'_n$. If not, then we reduce the step of iteration. In other words, we choose $\mathbf{r}_n = \mathbf{r}_{n-1} + 2^{-m}[\mathbf{r}'_n - \mathbf{r}_{n-1}]$ with $m \geq 1$ the smallest integer such that $\Gamma^{\mathbf{r}_n}$ is enclosed between Γ_i and Γ_e.

If the iterative solutions $\Gamma^{\mathbf{r}'_n}$ stay between Γ_i and Γ_e and if the steps of iteration $[\mathbf{r}'_n - \mathbf{r}_{n-1}]$ are small, then we fix the actual Γ_i and Γ_e and perform a larger number of Gauss–Newton steps.Applying this strategy to the

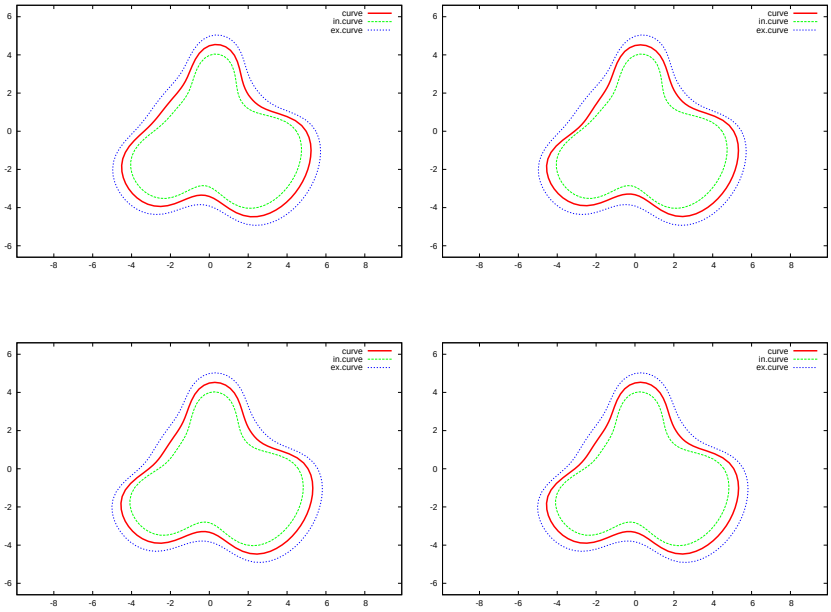

FIGURE 11. Kirsch–Kress steps 9-10 to reconstruct nonconvex domain.

reconstruction of our nonconvex domain, we need 9 Gauss–Newton steps with updated Γ_i and Γ_e and a final Gauss–Newton step (7 iterations) with fixed Γ_i and Γ_e. The Kirsch–Kress method reduces the initial deviation $\|\widetilde{\mathbf{r}} - \widetilde{\mathbf{r}}_{ini}\|_{L^\infty[0,2\pi]} = 1.57$ to a reconstruction accuracy $\|\widetilde{\mathbf{r}} - \widetilde{\mathbf{r}}_{KK}\|_{L^\infty[0,2\pi]} = 0.00032$. The initial solutions and the next iterative solutions of each step are shown in Figures 9–11.

5.5. **Reconstruction of curve with reduced number of nonzero Fourier coefficients.** Surely, one reason for the good reconstruction is that the boundary of the unknown obstacle (cf. (16) and (17)) can be exactly represented by the numerical ansatz for the parametrization including ten nonzero Fourier coefficients (cf. (26) and (27)). In many applications, the boundary of the obstacle can only be approximated by the numerical ansatz. To check our method for such a situation, we have slightly modified the nonconvex curve by adding the small Fourier coefficients

$$\widehat{a}_6 = 0.004, \quad \widehat{a}_7 = 0.001, \quad \widehat{b}_6 = -0.004, \quad \widehat{b}_7 = 0.001$$

to the set of nonzero coefficients in (27). With this boundary curve, we have generated far-field data. For the numerical reconstruction, however, we still use the ten nonzero Fourier coefficients $\widehat{a}_i$, $\widehat{b}_i$, $i = 1, \ldots, 5$. Note that the radial deviation of the unknown curve with fourteen nonzero coefficients from that with the ten is 0.0075. The reconstruction error for the simple Newton iteration is shown in Table 3 and is only slightly larger then that in

the right Table 1. Note that the initial solution for the results of Table 3 was chosen as $\widehat{a}_i^0 := 0.75\widehat{a}_i$ and $\widehat{b}_i^0 := 0.75\widehat{b}_i$, $i = 1, \ldots, 5$. A reconstruction with a similar accuracy but starting from the initial solution $\widehat{a}_i^0 := 0$ and $\widehat{b}_i^0 := 0$ was possible only over the finest grid with meshsize $h = 0.03125$. If the far-field data for the nonconvex obstacle with the fourteen nonzero Fourier coefficients is used in the Kirsch–Kress method based on ten nonzero Fourier coefficients, then the starting error 0.296 of the initial solution (cf. the left picture in Figure 8) is reduced to 0.00898 after 12 iterations.

h		0.5	0.25	0.125	0.0625	0.03125
err	1.57	0.1147	0.03812	0.01878	0.01688	0.01678
it	0	7	8	7	7	7

TABLE 3. Reconstruction of nonconvex domain by simple Newton iteration, far-field data generated from 14 Fourier coefficients.

5.6. **Reconstruction of obstacle with Jones mode.** Next we check the convergence of our methods in the case of a domain with Jones modes. For $r_J^0 = 5.135622\ldots$ as well as ω, μ, and ϱ from (15), we reconstruct the disk $\Omega_J := \{x \in \mathbb{R}^2 : \ |x| < r_J\}$, $r_J = \frac{1}{\omega}\sqrt{\mu/\varrho}\ r_J^0$ (cf. the Jones mode in (7)). We choose the curves $\Gamma_i = \Gamma^{\mathbf{r}_i}$ and $\Gamma_e = \Gamma^{\mathbf{r}_e}$ by $\mathbf{r}_i = r_J - 2$, $\mathbf{r}_e = r_J + 2$, and define the initial solution by (27). The initial and the true solution curves are shown in Figure 12. Applying the Kirsch–Kress algorithm with 176 discretization points per curve, with $\gamma = 4 \cdot 10^{-14}$, and with the scaling constants $c = 200$, $c_{\mathbf{r}} = 200$, $c_i = 5$, $c_e = 0.05$, the true solution is reconstructed after 8 iterations. The starting error 1.26 of the initial solution is reduced to 0.000814. The simple Newton type iteration method should converge only, if the included solver of the direct problem provides a partial solution for domains with Jones modes and an accurate solution for domains close to domains with Jones modes. In particular, an iterative solver might diverge. We have employed the direct solver of [22]. Due to discretization errors, the FEM matrices have small eigenvalues, but are not singular. The stable solver provides good solutions, and the simple Newton type iteration converges even for the reconstruction of the domain Ω_J. Choosing the regularization parameter $\gamma = 0$, we get a reconstruction accuracy of 0.000492 after 13 iterations.

5.7. **Noisy far-field data.** Finally, we have checked perturbed far-field data. For different values of ε, we have added a random number, uniformly distributed in $[-\varepsilon, \varepsilon]$, to the far-field values of the egg shaped domain. Tables 4 show the reconstruction accuracy depending on ε for the simple Newton iteration with FEM stepsize 0.03125 and for the Kirsch–Kress method

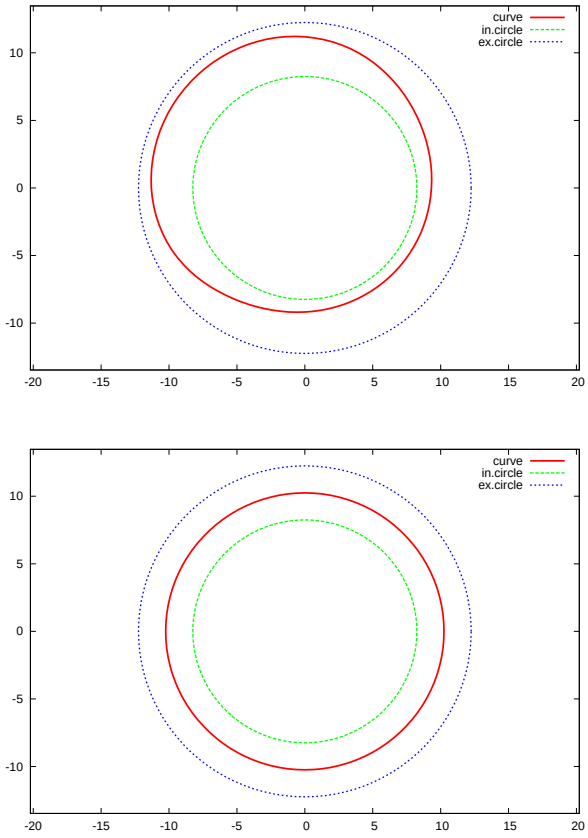

FIGURE 12. Initial solution with Fourier coefficients (27) and disk with Jones frequency.

with a number of discretization points $M = M' = 44$, respectively. Obviously, the simple Newton iteration is much more robust with respect to random perturbations. For the Kirsch–Kress method with $M = M' = 352$ points applied to the nonconvex domain (cf. Figure 8), the test results are shown in Table 5.

5.8. **Conclusions.** Summarizing the results, the advantage of the Kirsch–Kress method is the high accuracy of reconstruction for obstacles with smooth boundaries and, consequently, the fast computation time. Moreover, the method works well even if domains with Jones mode solutions appear. Note that the simple Newton method is based on the solution of the direct problem, which leads to singular or almost singular linear systems if the domain is an obstacle having Jones modes or if it is close to such an obstacle. The solver for this system must return a particular solution. An iterative scheme with preconditioner might diverge.

ε	$\|\widetilde{\mathbf{r}} - \widetilde{\mathbf{r}}_{FEM}\|_{L^\infty}$
0.	0.001568
0.001	0.002637
0.005	0.007156
0.01	0.01368
0.05	0.05433
0.1	0.1087
0.2	0.2339

ε	γ	$\|\widetilde{\mathbf{r}} - \widetilde{\mathbf{r}}_{KK}\|_{L^\infty}$
0.	$0.25 \cdot 10^{-12}$	0.002136
0.0001	$0.25 \cdot 10^{-10}$	0.003640
0.001	$0.25 \cdot 10^{-7}$	0.02041
0.003	$0.25 \cdot 10^{-6}$	0.05686
0.005	$1 \cdot 10^{-6}$	0.09997

TABLE 4. Reconstruction error of the egg shaped domain depending on the stochastic perturbation of the far-field data for simple Newton iteration and $\gamma = 0$ (left) and for Kirsch–Kress method (right).

ε	γ	$\|\|\widetilde{\mathbf{r}} - \widetilde{\mathbf{r}}_{KK}\|\|_{L^\infty}$	it
0.00000	10^{-8}	0.00028	11
0.00010	10^{-8}	0.0141	13
0.00025	10^{-8}	0.0345	11
0.00100	10^{-8}	0.113	8
0.00250	10^{-6}	0.187	9

TABLE 5. Reconstruction error of the Kirsch–Kress method depending on the stochastic perturbation of the far-field data, nonconvex domain.

Unfortunately, a successful run of the Kirsch–Kress method requires an optimal choice of the scaling constants. Additionally, the curves for the potential representations must be chosen properly, i.e., sufficiently close to the boundary of the iterative solution or to the boundary of the true obstacle. Heuristically, the closeness requirement depends on the degree of smoothness measured by the norms of analyticity of the parametrization functions. Eventually, the curves of the potential representation must be updated during the iteration. However, the closer these curves are the larger is the number of subdivision points and the number of degrees of freedom needed for the numerical discretization. The actual curves for the potential representation, the actual scaling constants, and the actual number of discretization points should be determined beforehand by test computations for known obstacles. A final disadvantage of the Kirsch–Kress method is its higher sensitivity with respect to noisy far-field data.

6. Derivatives of the 2D Discretized Objective Functional

6.1. **Derivatives of the points at the parameterized curve and of the normal vector with respect to the Fourier coefficients.** To define

the objective functional of the discretized optimization problem (cf. (A.6)) and to get formulas for its derivatives, we need formulas for the parametrization, the normal, the incoming wave, the Green kernels, and for their derivatives. Since the derivation is straightforward, we only present the results.

Here we start with formulas for the parameterization point $x_{\mathbf{r}}(\zeta) := \widetilde{\mathbf{r}}(\zeta)\exp(\mathbf{i}\zeta)$ (cf. 17) on the approximate interface, for the normal ν at $x_{\mathbf{r},\kappa}$, and for their derivatives with respect to the Fourier coefficients. Clearly, the set of coefficients is to be truncated such that we can compute with a finite set of parameters $\{\widehat{a}_0, \widehat{a}_j, \widehat{b}_j : \ j = 1, 2, \ldots, n\}$. To simplify the formulas, we set $N = 2n+1$ and collect these Fourier coefficients in the set $\{a_\iota : \ \iota \in I_N\}$ and write the parametric representation as

$$x_{\mathbf{r}}(\zeta) := \mathbf{r}(\zeta)e^{\mathbf{i}\zeta}, \quad \mathbf{r}(\zeta) := \frac{r_e + r_i}{2} + \frac{r_e - r_i}{\pi} \arctan\Big(\sum_{\iota\in I_N} a_\iota \psi_\iota(\zeta)\Big). \quad \text{(A.1)}$$

Here $\psi_\iota(\zeta) = \cos(j\zeta)$ if $a_\iota = \widehat{a}_j$ and $\psi_\iota(\zeta) = \sin(j\zeta)$ if $a_\iota = \widehat{b}_j$. For the derivatives, we arrive at

$$\begin{aligned}
\mathbf{r}'(\zeta) &= \frac{r_e - r_i}{\pi} \frac{\sum\limits_{\iota\in I_N} a_\iota \psi_\iota'(\zeta)}{1 + \big(\sum\limits_{\iota\in I_N} a_\iota \psi_\iota(\zeta)\big)^2}, \\
\frac{\partial}{\partial a_\iota}\, \mathbf{r}(\zeta) &= \frac{r_e - r_i}{\pi} \frac{\psi_\iota(\zeta)}{1 + \big(\sum\limits_{\iota'\in I_N} a_{\iota'} \psi_{\iota'}(\zeta)\big)^2}, \\
\frac{\partial}{\partial a_\iota}\, x_{\mathbf{r}}(\zeta) &= \frac{r_e - r_i}{\pi} \frac{\psi_\iota(\zeta)}{1 + \big(\sum\limits_{\iota'\in I_N} a_{\iota'} \psi_{\iota'}(\zeta)\big)^2} e^{i\zeta}, \\
\frac{\partial}{\partial a_\iota}\, \mathbf{r}'(\zeta) &= \frac{r_e - r_i}{\pi} \frac{\psi_\iota'(\zeta)}{1 + \big(\sum\limits_{\iota'\in I_N} a_{\iota'} \psi_{\iota'}(\zeta)\big)^2} - \\
&\qquad - 2\,\frac{r_e - r_i}{\pi} \frac{\big[\sum\limits_{\iota'\in I_N} a_{\iota'} \psi_{\iota'}'(\zeta)\big] \big[\sum\limits_{\iota'\in I_N} a_{\iota'} \psi_{\iota'}(\zeta)\big] \psi_\iota(\zeta)}{\big[1 + \big(\sum\limits_{\iota'\in I_N} a_{\iota'} \psi_{\iota'}(\zeta)\big)^2\big]^2}.
\end{aligned}$$

A normal $\widetilde{\nu}$ to the curve at $x_{\mathbf{r}}(\zeta)$ and the unit normal ν are given by

$$\begin{aligned}
\widetilde{\nu}(x_{\mathbf{r}}(\zeta)) &= e^{-\mathbf{i}\pi/2} \frac{\partial}{\partial\zeta} \big[x_{\mathbf{r}}(\zeta)\big] = e^{-\mathbf{i}\pi/2} \frac{\partial}{\partial\zeta} \big[\mathbf{r}(\zeta)e^{\mathbf{i}\zeta}\big] = \\
&= e^{-\mathbf{i}\pi/2} \Big[\mathbf{r}'(\zeta)e^{\mathbf{i}\zeta} + \mathbf{r}(\zeta)e^{\mathbf{i}\pi/2}e^{\mathbf{i}\zeta}\Big] = \\
&= \Big[e^{-\mathbf{i}\pi/2}\mathbf{r}'(\zeta) + \mathbf{r}(\zeta)\Big] e^{\mathbf{i}\zeta}, \\
\nu(x_{\mathbf{r}}(\zeta)) &= \frac{\big[e^{-\mathbf{i}\pi/2}\mathbf{r}'(\zeta) + \mathbf{r}(\zeta)\big] e^{\mathbf{i}\zeta}}{\big|e^{-\mathbf{i}\pi/2}\mathbf{r}'(\zeta) + \mathbf{r}(\zeta)\big|} = \frac{\mathbf{r}'(\zeta)e^{\mathbf{i}(\zeta-\pi/2)} + \mathbf{r}(\zeta)e^{\mathbf{i}\zeta}}{\mathbf{s}(\zeta)}, \qquad \text{(A.2)} \\
\mathbf{s}(\zeta) &:= \sqrt{\mathbf{r}'(\zeta)^2 + \mathbf{r}(\zeta)^2}. \qquad \text{(A.3)}
\end{aligned}$$

The derivatives of these entities can be computed by the formulas

$$\frac{\partial}{\partial a_\iota}\,\nu(x_{\mathbf{r}}(\zeta)) = \frac{\partial}{\partial a_\iota}\,\frac{\mathbf{r}'(\zeta)}{\mathbf{s}(\zeta)}\,e^{\mathbf{i}(\zeta-\pi/2)} + \frac{\partial}{\partial a_\iota}\,\frac{\mathbf{r}(\zeta)}{\mathbf{s}(\zeta)}\,e^{\mathbf{i}\zeta}\,,$$

$$\frac{\partial}{\partial a_\iota}\,\frac{\mathbf{r}'(\zeta)}{\mathbf{s}(\zeta)} = \frac{\partial_{a_\iota}\mathbf{r}'(\zeta)}{\mathbf{s}(\zeta)} - \frac{1}{2}\,\frac{\mathbf{r}'(\zeta)\big\{2\mathbf{r}'(\zeta)\partial_{a_\iota}\mathbf{r}'(\zeta)+2\mathbf{r}(\zeta)\partial_{a_\iota}\mathbf{r}(\zeta)\big\}}{\mathbf{s}(\zeta)^3} =$$

$$= \frac{\partial_{a_\iota}\mathbf{r}'(\zeta)}{\mathbf{s}(\zeta)} - \frac{\mathbf{r}'(\zeta)\big\{\mathbf{r}'(\zeta)\partial_{a_\iota}\mathbf{r}'(\zeta)+\mathbf{r}(\zeta)\partial_{a_\iota}\mathbf{r}(\zeta)\big\}}{\mathbf{s}(\zeta)^3}\,,$$

$$\frac{\partial}{\partial a_\iota}\,\frac{\mathbf{r}(\zeta)}{\mathbf{s}(\zeta)} = \frac{\partial_{a_\iota}\mathbf{r}(\zeta)}{\mathbf{s}(\zeta)} - \frac{\mathbf{r}(\zeta)\big\{\mathbf{r}'(\zeta)\partial_{a_\iota}\mathbf{r}'(\zeta)+\mathbf{r}(\zeta)\partial_{a_\iota}\mathbf{r}(\zeta)\big\}}{\mathbf{s}(\zeta)^3}\,.$$

6.2. **Values and derivatives of incoming wave and kernel functions.** Suppose v^{inc} is the direction of the incoming wave, then

$$p^{inc}(x) = e^{\mathbf{i}k_\omega v^{inc}\cdot x}\,,$$

$$\partial_{x_j}p^{inc}(x) = \mathbf{i}k_\omega e^{\mathbf{i}k_\omega v^{inc}\cdot x}[v^{inc}]_j\,,$$

$$\partial_{x_j}\partial_{x_l}p^{inc}(x) = -k_\omega^2 e^{\mathbf{i}k_\omega v^{inc}\cdot x}[v^{inc}]_j[v^{inc}]_l.$$

For the derivatives of the acoustic Green kernel, we obtain (cf. [1])

$$G\big(x,y\big) = \frac{\mathbf{i}}{4}\,H_0^{(1)}(k|x-y|),$$

$$H_0^{(1)}(t) := J_0(t)+\mathbf{i}Y_0(t),$$

$$\partial_{x_j}G\big(x,y\big) = \frac{\mathbf{i}k}{4}\,[H_0^{(1)}]'(k|x-y|)\,\frac{(x_j-y_j)}{|x-y|}\,,$$

$$[H_0^{(1)}]'(t) := -J_1(t)-\mathbf{i}Y_1(t),$$

$$\partial_{y_j}G\big(x,y\big) = \frac{\mathbf{i}k}{4}\,[H_0^{(1)}]'(k|x-y|)\,\frac{(y_j-x_j)}{|x-y|}\,,$$

$$\partial_{x_j}\partial_{x_l}G\big(x,y\big) = \frac{\mathbf{i}k}{4}\,[H_0^{(1)}]'(k|x-y|)\,\frac{|x-y|^2\delta_{j,l}-2(x_j-y_j)(x_l-y_l)}{|x-y|^3}\,,$$

$$-\frac{\mathbf{i}k^2}{4}\,H_0^{(1)}(k|x-y|)\,\frac{(x_j-y_j)(x_l-y_l)}{|x-y|^2}\,.$$

For the third order derivatives, we observe

$$\partial_{x_m}\partial_{x_j}\partial_{x_l}G\big(x,y\big) =$$

$$= \mathbf{i}k^2H_0^{(1)}(k|x-y|)\Big\{\frac{(x_j-y_j)(x_l-y_l)(x_m-y_m)}{|x-y|^4}-$$

$$-\frac{(x_m-y_m)\delta_{j,l}+(x_l-y_l)\delta_{j,m}+(x_j-y_j)\delta_{l,m}}{4|x-y|^2}\Big\}+$$

$$+\frac{\mathbf{i}k}{2}[H_0^{(1)}]'(k|x-y|)\Big\{\frac{(x_m-y_m)(x_j-y_j)(x_l-y_l)}{2|x-y|^5}\,\big[8-k^2|x-y|^2\big]-$$

$$-\frac{(x_m-y_m)\delta_{j,l}+(x_l-y_l)\delta_{j,m}+(x_j-y_j)\delta_{l,m}}{|x-y|^3}\Bigg\},$$

$$\partial_{y_m}\partial_{x_j}\partial_{x_l}G\big(x,y\big)=$$

$$=\mathbf{i}k^2H_0^{(1)}(k|x-y|)\Bigg\{\frac{(y_j-x_j)(y_l-x_l)(y_m-x_m)}{|x-y|^4}-$$

$$-\frac{(y_m-x_m)\delta_{j,l}+(y_l-x_l)\delta_{j,m}+(y_j-x_j)\delta_{l,m}}{4|x-y|^2}\Bigg\}+$$

$$+\frac{\mathbf{i}k}{2}[H_0^{(1)}]'(k|x-y|)\Bigg\{\frac{(y_m-x_m)(y_j-x_j)(y_l-x_l)}{2|x-y|^5}\left[8-k^2|x-y|^2\right]-$$

$$-\frac{(y_m-x_m)\delta_{j,l}+(y_l-x_l)\delta_{j,m}+(y_j-x_j)\delta_{l,m}}{|x-y|^3}\Bigg\}.$$

The fourth order derivatives take the form

$$\partial_{y_n}\partial_{y_m}\partial_{x_j}\partial_{x_l}G\big(x,y\big)=\mathbf{i}k^2H_0^{(1)}(k|x-y|)\times$$

$$\times\Bigg\{\frac{(y_l-x_l)(y_m-x_m)\delta_{n,j}}{|x-y|^4}+\frac{(y_j-x_j)(y_m-x_m)\delta_{n,l}}{|x-y|^4}+$$

$$+\frac{(y_j-x_j)(y_l-x_l)\delta_{n,m}}{|x-y|^4}-\frac{\delta_{j,l}\delta_{n,m}+\delta_{j,m}\delta_{n,l}+\delta_{l,m}\delta_{n,j}}{4|x-y|^2}+$$

$$+(y_n-x_n)\,\frac{(y_m-x_m)\delta_{j,l}+(y_l-x_l)\delta_{j,m}+(y_j-x_j)\delta_{l,m}}{|x-y|^4}-$$

$$-\frac{(y_n-x_n)(y_m-x_m)(y_j-x_j)(y_l-x_l)}{4|x-y|^6}\left[24-k^2|x-y|^2\right]\Bigg\}+$$

$$+\mathbf{i}k[H_0^{(1)}]'(k|x-y|)\times$$

$$\times\Bigg\{\left[2k^2|x-y|^2-12\right]\frac{(y_j-x_j)(y_l-x_l)(y_m-x_m)(y_n-x_n)}{|x-y|^7}+$$

$$+[8-k^2|y-x|^2]\times$$

$$\times(y_n-x_n)\frac{(y_m-x_m)\delta_{j,l}+(y_l-x_l)\delta_{j,m}+(y_j-x_j)\delta_{l,m}}{4|x-y|^5}+$$

$$+\left[8-k^2|x-y|^2\right]\times$$

$$\times\frac{(y_j-x_j)(y_l-x_l)\delta_{n,m}+(y_m-x_m)(y_l-x_l)\delta_{n,j}\delta_{n,l}}{4|x-y|^5}+$$

$$+\left[8-k^2|x-y|^2\right]\frac{(y_m-x_m)(y_j-x_j)\delta_{n,l}}{4|x-y|^5}-$$

$$-\frac{\delta_{j,l}\delta_{n,m}+\delta_{j,m}\delta_{n,l}+\delta_{l,m}\delta_{n,j}}{2|x-y|^3}\Bigg\}.$$

For the derivatives of the elastic Green kernel, we conclude

$$
\begin{aligned}
[G^{el}(x,y)]_{j,l} &= \frac{1}{\mu}\, G(x,y;k_s)\delta_{j,l} + \frac{1}{\mu k_s^2}\,\partial_{x_j}\partial_{x_l} G(x,y;k_s) - \\
&\quad - \frac{1}{\mu k_s^2}\,\partial_{x_j}\partial_{x_l} G(x,y;k_p), \\
\partial_{y_m}[G^{el}(x,y)]_{j,l} &= \frac{1}{\mu}\,\partial_{y_m} G(x,y;k_s)\delta_{j,l} + \frac{1}{\mu k_s^2}\,\partial_{y_m}\partial_{x_j}\partial_{x_l} G(x,y;k_s) - \\
&\quad - \frac{1}{\mu k_s^2}\,\partial_{y_m}\partial_{x_j}\partial_{x_l} G(x,y;k_p), \\
\partial_{y_n}\partial_{y_m}[G^{el}(x,y)]_{j,l} &= \frac{1}{\mu}\,\partial_{y_n}\partial_{y_m} G(x,y;k_s)\delta_{j,l} + \\
&\quad + \frac{1}{\mu k_s^2}\,\partial_{y_n}\partial_{y_m}\partial_{x_j}\partial_{x_l} G(x,y;k_s) - \\
&\quad - \frac{1}{\mu k_s^2}\,\partial_{y_n}\partial_{y_m}\partial_{x_j}\partial_{x_l} G(x,y;k_p), \\
t_y[G^{el}(x,y)]_{\cdot,l} &= 2\mu \begin{pmatrix} \sum\limits_{j=1}^{2} \nu_j \partial_{y_j}[G^{el}(x,y)]_{1,l} \\ \sum\limits_{j=1}^{2} \nu_j \partial_{y_j}[G^{el}(x,y)]_{2,l} \end{pmatrix} + \\
&\quad + \lambda\Big[\partial_{y_1}[G^{el}(x,y)]_{1,l} + \partial_{y_2}[G^{el}(x,y)]_{2,l}\Big]\nu + \\
&\quad + \mu \begin{pmatrix} \nu_2\Big(\partial_{y_1}[G^{el}(x,y)]_{2,l} - \partial_{y_2}[G^{el}(x,y)]_{1,l}\Big) \\ \nu_1\Big(\partial_{y_2}[G^{el}(x,y)]_{1,l} - \partial_{y_1}[G^{el}(x,y)]_{2,l}\Big) \end{pmatrix}, \\
\partial_{y_m} t_y[G^{el}(x,y)]_{\cdot,l} &= 2\mu \begin{pmatrix} \sum\limits_{j=1}^{2} \nu_j \partial_{y_m}\partial_{y_j}[G^{el}(x,y)]_{1,l} \\ \sum\limits_{j=1}^{2} \nu_j \partial_{y_m}\partial_{y_j}[G^{el}(x,y)]_{2,l} \end{pmatrix} + \\
&\quad + \lambda\Big[\partial_{y_m}\partial_{y_1}[G^{el}(x,y)]_{1,l} + \partial_{y_m}\partial_{y_2}[G^{el}(x,y)]_{2,l}\Big]\nu + \\
&\quad + \mu \begin{pmatrix} \nu_2\Big(\partial_{y_m}\partial_{y_1}[G^{el}(x,y)]_{2,l} - \partial_{y_m}\partial_{y_2}[G^{el}(x,y)]_{1,l}\Big) \\ \nu_1\Big(\partial_{y_m}\partial_{y_2}[G^{el}(x,y)]_{1,l} - \partial_{y_m}\partial_{y_1}[G^{el}(x,y)]_{2,l}\Big) \end{pmatrix}, \\
\partial_{\nu_m} t_y[G^{el}(x,y)]_{\cdot,l} &= 2\mu \begin{pmatrix} \partial_{y_m}[G^{el}(x,y)]_{1,l} \\ \partial_{y_m}[G^{el}(x,y)]_{2,l} \end{pmatrix} + \\
&\quad + \lambda\Big[\partial_{y_1}[G^{el}(x,y)]_{1,l} + \partial_{y_2}[G^{el}(x,y)]_{2,l}\Big] \begin{pmatrix} \delta_{1,m} \\ \delta_{2,m} \end{pmatrix} +
\end{aligned}
$$

$$+\mu\begin{pmatrix}\delta_{2,m}\Big(\partial_{y_1}[G^{el}(x,y)]_{2,l}-\partial_{y_2}[G^{el}(x,y)]_{1,l}\Big)\\ \delta_{1,m}\Big(\partial_{y_2}[G^{el}(x,y)]_{1,l}-\partial_{y_1}[G^{el}(x,y)]_{2,l}\Big)\end{pmatrix}.$$

6.3. **Least squares approach for the Gauss-Newton algorithm.** Suppose I_N is the index set of the Fourier coefficients from 6.1 and the layer functions of the Kirsch–Kress method are approximated by (23), (24). Furthermore, suppose the L^2 norms on $\Gamma^{\mathbf{r}}$ and $[0,2\pi]$ in $\mathcal{J}^3_\gamma$ are discretized by

$$\|f\|^2_{L^2(\Gamma^{\mathbf{r}})}\sim\sum_{\kappa=1}^{M'}\big|f(x_{\mathbf{r},\kappa})\big|^2,\quad x_{\mathbf{r},\kappa}:=\mathbf{r}(\tau_\kappa)e^{\mathbf{i}\tau_\kappa},\quad \tau_\kappa:=\frac{2\pi\kappa}{M'}\,,\tag{A.4}$$

$$\|g\|^2_{L^2[0,2\pi]}\sim\sum_{\kappa=1}^{M''}\big|g(\sigma_\kappa)\big|^2,\quad \sigma_\kappa:=\frac{2\pi\kappa}{M''}\,.\tag{A.5}$$

Then the discretized objective functional for (21) is of the form

$$\mathcal{J}_{N,M,M',\gamma}\big(\varphi_{i,M},\vec{\varphi}_{e,M},\mathbf{r}_N\big)=\Big\|\mathcal{M}\big((b_\kappa)_{\kappa=1}^M,(c_\kappa)_{\kappa=1}^M,(a_\iota)_{\iota\in I_N}\big)-\mathcal{R}\Big\|^2_{\ell^2},\tag{A.6}$$

$$\mathcal{M}:=\Big((\mathcal{M}_{1,\kappa}),(\mathcal{M}_{2,\kappa}),(\mathcal{M}_{3,\kappa,l}),(\mathcal{M}_{4,\kappa,l}),(\mathcal{M}_{5,\kappa})\Big),$$

$$\mathcal{R}:=\Big((\mathcal{R}_{1,\kappa}),(\mathcal{R}_{2,\kappa}),(\mathcal{R}_{3,\kappa,l}),(\mathcal{R}_{4,\kappa,l}),(\mathcal{R}_{5,\kappa})\Big),$$

where

$$\begin{aligned}\mathcal{R}_{1,\kappa}&:=\frac{1}{\sqrt{M''}}\,p^\infty_{noisy}(\sigma_{\kappa'}),\\ \mathcal{R}_{2,\kappa'}&:=0,\\ \mathcal{R}_{3,\kappa',l}&:=0,\\ \mathcal{R}_{4,\kappa',l}&:=0,\\ \mathcal{R}_{5,\kappa'}&:=0,\end{aligned}\tag{A.7}$$

$$\mathcal{M}\big((b_\kappa),(c_\kappa),(a_\iota)\big)_{1,\kappa'}:=\frac{e^{\mathbf{i}\pi/4}}{\sqrt{8\pi k_\omega}\sqrt{M''}}\sum_{\kappa=1}^{M}b_\kappa e^{-\mathbf{i}k_\omega\exp(\mathbf{i}\sigma_{\kappa'})\cdot x_{i,\kappa}},\tag{A.8}$$
$$\kappa'=1,\dots,M'',$$

$$\mathcal{M}\big((b_\kappa),(c_\kappa),(a_\iota)\big)_{2,\kappa'}:=\frac{\sqrt{\gamma}}{\sqrt{M}}\sum_{\kappa=1}^{M}\log\sin^2\Big(\frac{\pi[\kappa'-\kappa]}{M}\Big)b_\kappa,\tag{A.9}$$
$$\kappa'=1,\dots,M,$$

$$\mathcal{M}\big((b_\kappa),(c_\kappa),(a_\iota)\big)_{3,\kappa',l}:=\frac{\sqrt{\gamma}}{\sqrt{M}}\sum_{\kappa=1}^{M}\log\sin^2\Big(\frac{\pi[\kappa'-\kappa]}{M}\Big)[c_\kappa]_l,\tag{A.10}$$
$$\kappa'=1,\dots,M,\quad l=1,2,$$

$$\mathcal{M}\big((b_\kappa),(c_\kappa),(a_\iota)\big)_{4,\kappa',l} := \frac{1}{\sqrt{M'}}\sum_{\kappa=1}^{M}\Big[t_{x_{\mathbf{r},\kappa'}}\big[G^{el}(x_{e,\kappa},x_{\mathbf{r},\kappa'})c_\kappa\big]\Big]_l + \\ + \frac{1}{\sqrt{M'}}\sum_{\kappa=1}^{M} b_\kappa G\big(x_{\mathbf{r},\kappa'},x_{i,\kappa}\big)\big[\nu(x_{\mathbf{r},\kappa'})\big]_l + \\ + \frac{p^{inc}(x_{\mathbf{r},\kappa'})[\nu(x_{\mathbf{r},\kappa'})]_l}{\sqrt{M'}}\,, \qquad \text{(A.11)}$$
$$\kappa' = 1,\dots,M',\ \ l=1,2,$$

$$\mathcal{M}\big((b_\kappa),(c_\kappa),(a_\iota)\big)_{5,\kappa'} := \frac{1}{\sqrt{M'}}\sum_{\kappa=1}^{M}\nu(x_{\mathbf{r},\kappa'})\cdot G^{el}(x_{e,\kappa},x_{\mathbf{r},\kappa'})c_\kappa - \\ - \frac{1}{\sqrt{M'}\,\varrho_f\omega^2}\sum_{\kappa=1}^{M} b_\kappa\partial_{\nu(x_{\mathbf{r},\kappa'})}G(x_{\mathbf{r},\kappa'},x_{i,\kappa}) - \\ - \frac{\partial_\nu p^{inc}(x_{\mathbf{r},\kappa'})}{\sqrt{M'}\,\varrho_f\omega^2},\ \ \kappa'=1,\dots,M'. \qquad \text{(A.12)}$$

Here we define the expression $\{\log\sin^2(\pi 0/M)\}$ as 0. This leads to the following formulas for the derivatives. For the first components, we get

$$\frac{\partial}{\partial[\Re\mathrm{e}\,b_\kappa]}\mathcal{M}\big((b_\kappa),(c_\kappa),(a_\iota)\big)_{1,\kappa'} = \frac{e^{\mathbf{i}\pi/4}}{\sqrt{8\pi k_\omega}\sqrt{M''}}\begin{pmatrix}\cos\big(-k_\omega e^{\mathbf{i}\sigma_{\kappa'}}\cdot x_{i,\kappa}\big)\\ \sin\big(-k_\omega e^{\mathbf{i}\sigma_{\kappa'}}\cdot x_{i,\kappa}\big)\end{pmatrix}^\top,$$
$$\frac{\partial}{\partial[\Im\mathrm{m}\,b_\kappa]}\mathcal{M}\big((b_\kappa),(c_\kappa),(a_\iota)\big)_{1,\kappa'} = \frac{e^{\mathbf{i}\pi/4}}{\sqrt{8\pi k_\omega}\sqrt{M''}}\begin{pmatrix}-\sin\big(-k_\omega e^{\mathbf{i}\sigma_{\kappa'}}\cdot x_{i,\kappa}\big)\\ \cos\big(-k_\omega e^{\mathbf{i}\sigma_{\kappa'}}\cdot x_{i,\kappa}\big)\end{pmatrix}^\top.$$

For the second components, we obtain

$$\frac{\partial}{\partial[\Re\mathrm{e}\,b_\kappa]}\mathcal{M}\big((b_\kappa),(c_\kappa),(a_\iota)\big)_{2,\kappa'} = \frac{\sqrt{\gamma}}{\sqrt{M}}\begin{pmatrix}\log\sin^2\Big(\dfrac{\pi[\kappa'-\kappa]}{M}\Big)\\ 0\end{pmatrix}^\top,$$
$$\frac{\partial}{\partial[\Im\mathrm{m}\,b_\kappa]}\mathcal{M}\big((b_\kappa),(c_\kappa),(a_\iota)\big)_{2,\kappa'} = \frac{\sqrt{\gamma}}{\sqrt{M}}\begin{pmatrix}0\\ \log\sin^2\Big(\dfrac{\pi[\kappa'-\kappa]}{M}\Big)\end{pmatrix}^\top.$$

For the third components, we have

$$\frac{\partial}{\partial[\Re\mathrm{e}\,[c_\kappa]_l]}\mathcal{M}\big((b_\kappa),(c_\kappa),(a_\iota)\big)_{3,\kappa',l'} = \frac{\sqrt{\gamma}}{\sqrt{M}}\begin{pmatrix}\log\sin^2(\dfrac{\pi[\kappa'-\kappa]}{M})\delta_{l,l'}\\ 0\end{pmatrix}^\top,$$
$$\frac{\partial}{\partial[\Im\mathrm{m}\,[c_\kappa]_l]}\mathcal{M}\big((b_\kappa),(c_\kappa),(a_\iota)\big)_{3,\kappa',l'} = \frac{\sqrt{\gamma}}{\sqrt{M}}\begin{pmatrix}0\\ \log\sin^2\Big(\dfrac{\pi[\kappa'-\kappa]}{M}\Big)\delta_{l,l'}\end{pmatrix}^\top.$$

The derivatives of the fourth components take the form

$$\frac{\partial}{\partial[\Re\mathrm{e}\, b_\kappa]}\,\mathcal{M}\big((b_\kappa),(c_\kappa),(a_\iota)\big)_{4,\kappa',l} =$$
$$= \frac{1}{\sqrt{M'}} \begin{pmatrix} \Re\mathrm{e}\, G(x_{\mathbf{r},\kappa'}, x_{i,\kappa})[\nu(x_{\mathbf{r},\kappa'})]_l \\ \Im\mathrm{m}\, G(x_{\mathbf{r},\kappa'}, x_{i,\kappa})[\nu(x_{\mathbf{r},\kappa'})]_l \end{pmatrix}^\top,$$
$$\frac{\partial}{\partial[\Im\mathrm{m}\, b_\kappa]}\,\mathcal{M}\big((b_\kappa),(c_\kappa),(a_\iota)\big)_{4,\kappa',l} =$$
$$= \frac{1}{\sqrt{M'}} \begin{pmatrix} -\Im\mathrm{m}\, G(x_{\mathbf{r},\kappa'}, x_{i,\kappa})[\nu(x_{\mathbf{r},\kappa'})]_l \\ \Re\mathrm{e}\, G(x_{\mathbf{r},\kappa'}, x_{i,\kappa})[\nu(x_{\mathbf{r},\kappa'})]_l \end{pmatrix}^\top,$$
$$\frac{\partial}{\partial[\Re\mathrm{e}\,[c_\kappa]_l]}\,\mathcal{M}\big((b_\kappa),(c_\kappa),(a_\iota)\big)_{4,\kappa',l'} =$$
$$= \frac{1}{\sqrt{M'}} \begin{pmatrix} \Big[t_{x_{\mathbf{r},\kappa'}}\Big(\big[\Re\mathrm{e}\, G^{el}(x_{e,\kappa}, x_{\mathbf{r},\kappa'})\big]_{m,l}\Big)_m\Big]_{l'} \\ \Big[t_{x_{\mathbf{r},\kappa'}}\Big(\big[\Im\mathrm{m}\, G^{el}(x_{e,\kappa}, x_{\mathbf{r},\kappa'})\big]_{m,l}\Big)_m\Big]_{l'} \end{pmatrix}^\top,$$
$$\frac{\partial}{\partial[\Im\mathrm{m}\,[c_\kappa]_l]}\,\mathcal{M}\big((b_\kappa),(c_\kappa),(a_\iota)\big)_{4,\kappa',l'} =$$
$$= \frac{1}{\sqrt{M'}} \begin{pmatrix} -\Big[t_{x_{\mathbf{r},\kappa'}}\Big(\big[\Im\mathrm{m}\, G^{el}(x_{e,\kappa}, x_{\mathbf{r},\kappa'})\big]_{m,l}\Big)_m\Big]_{l'} \\ \Big[t_{x_{\mathbf{r},\kappa'}}\Big(\big[\Re\mathrm{e}\, G^{el}(x_{e,\kappa}, x_{\mathbf{r},\kappa'})\big]_{m,l}\Big)_m\Big]_{l'} \end{pmatrix}^\top,$$
$$\frac{\partial}{\partial a_\iota}\,\mathcal{M}\big((b_\kappa),(c_\kappa),(a_\iota)\big)_{4,\kappa',l} =$$
$$= \frac{1}{\sqrt{M'}} \sum_{\kappa=1}^{M} \mathrm{grad}_{\,x_{\mathbf{r},\kappa'}}\Big[t_{x_{\mathbf{r},\kappa'}}\big[G^{el}(x_{e,\kappa}, x_{\mathbf{r},\kappa'})c_\kappa\big]\Big]_l \frac{\partial}{\partial a_\iota}[x_{\mathbf{r},\kappa'}] +$$
$$+ \frac{1}{\sqrt{M'}} \sum_{\kappa=1}^{M} b_\kappa \mathrm{grad}_{\,x_{\mathbf{r},\kappa'}}\big[G(x_{\mathbf{r},\kappa'}, x_{i,\kappa})\big] \frac{\partial}{\partial a_\iota}\,[x_{\mathbf{r},\kappa'}]\,\big[\nu(x_{\mathbf{r},\kappa'})\big]_l +$$
$$+ \frac{1}{\sqrt{M'}} \sum_{\kappa=1}^{M} b_\kappa G(x_{\mathbf{r},\kappa'}, x_{i,\kappa})\,\frac{\partial}{\partial a_\iota}\,[\nu(x_{\mathbf{r},\kappa'})]_l +$$
$$+ \frac{1}{\sqrt{M'}}\,\mathrm{grad}_{\,x_{\mathbf{r},\kappa'}}\big[p^{inc}(x_{\mathbf{r},\kappa'})\big]\,\frac{\partial}{\partial a_\iota}\,[x_{\mathbf{r},\kappa'}]\,\big[\nu(x_{\mathbf{r},\kappa'})\big]_l +$$
$$+ \frac{1}{\sqrt{\#K_{M'}}}\,p^{inc}(x_{\mathbf{r},\kappa'})\,\frac{\partial}{\partial a_\iota}\,\big[\nu(x_{\mathbf{r},\kappa'})\big]_l.$$

Finally, for the fifth components, we obtain

$$\frac{\partial}{\partial[\Re\mathrm{e}\, b_\kappa]}\,\mathcal{M}\big((b_\kappa),(c_\kappa),(a_\iota)\big)_{5,\kappa'} =$$

$$= -\frac{1}{\sqrt{M'}\,\varrho_f\omega^2}\begin{pmatrix}\partial_{\nu(x_{\mathbf{r},\kappa'})}\Re\mathrm{e}\,G(x_{\mathbf{r},\kappa'},x_{i,\kappa})\\ \partial_{\nu(x_{\mathbf{r},\kappa'})}\Im\mathrm{m}\,G(x_{\mathbf{r},\kappa'},x_{i,\kappa})\end{pmatrix}^{\top},$$

$$\frac{\partial}{\partial[\Im\mathrm{m}\,b_\kappa]}\,\mathcal{M}\big((b_\kappa),(c_\kappa),(a_\iota)\big)_{5,\kappa'} =$$

$$= -\frac{1}{\sqrt{M'}\,\varrho_f\omega^2}\begin{pmatrix}-\partial_{\nu(x_{\mathbf{r},\kappa'})}\Im\mathrm{m}\,G\big(x_{\mathbf{r},\kappa'},x_{i,\kappa}\big)\\ \partial_{\nu(x_{\mathbf{r},\kappa'})}\Re\mathrm{e}\,G\big(x_{\mathbf{r},\kappa'},x_{i,\kappa}\big)\end{pmatrix}^{\top},$$

$$\frac{\partial}{\partial[\Re\mathrm{e}\,[c_\kappa]_l]}\,\mathcal{M}\big((b_\kappa),(c_\kappa),(a_\iota)\big)_{5,\kappa'} =$$

$$= \frac{1}{\sqrt{M'}}\begin{pmatrix}\nu(x_{\mathbf{r},\kappa'})\cdot\Big(\Re\mathrm{e}\,\big[G^{el}(x_{\mathbf{r},\kappa'},x_{i,\kappa})\big]_{m,l}\Big)_m\\ \nu(x_{\mathbf{r},\kappa'})\cdot\Big(\Im\mathrm{m}\,\big[G^{el}(x_{\mathbf{r},\kappa'},x_{i,\kappa})\big]_{m,l}\Big)_m\end{pmatrix}^{\top},$$

$$\frac{\partial}{\partial[\Im\mathrm{m}\,[c_\kappa]_l]}\,\mathcal{M}\big((b_\kappa),(c_\kappa),(a_\iota)\big)_{5,\kappa'} =$$

$$= \frac{1}{\sqrt{M'}}\begin{pmatrix}-\nu(x_{\mathbf{r},\kappa'})\cdot\Big(\Im\mathrm{m}\,\big[G^{el}(x_{\mathbf{r},\kappa'},x_{i,\kappa})\big]_{m,l}\Big)_m\\ \nu(x_{\mathbf{r},\kappa'})\cdot\Big(\Re\mathrm{e}\,\big[G^{el}(x_{\mathbf{r},\kappa'},x_{i,\kappa})\big]_{m,l}\Big)_m\end{pmatrix}^{\top},$$

$$\frac{\partial}{\partial a_\iota}\,\mathcal{M}\big((b_\kappa),(c_\kappa),(a_\iota)\big)_{5,\kappa'} =$$

$$= \frac{1}{\sqrt{M'}}\sum_{\kappa=1}^{M}{}^{\top}\big[G^{el}(x_{e,\kappa},x_{\mathbf{r},\kappa'})c_\kappa\big]\,\frac{\partial}{\partial a_\iota}\,[\nu(x_{\mathbf{r},\kappa'})]+$$

$$+\frac{1}{\sqrt{M'}}\sum_{\kappa=1}^{M}\nu(x_{\mathbf{r},\kappa'})\cdot\mathrm{grad}_{\,x_{\mathbf{r},\kappa'}}\big[G^{el}(x_{e,\kappa},x_{\mathbf{r},\kappa'})c_\kappa\big]\,\frac{\partial}{\partial a_\iota}\,[x_{\mathbf{r},\kappa'}]-$$

$$-\frac{1}{\sqrt{M'}\,\varrho_f\omega^2}\sum_{\kappa=1}^{M}{}^{\top}\big[b_\kappa\mathrm{grad}_{\,x_{\mathbf{r},\kappa'}}G(x_{\mathbf{r},\kappa'},x_{i,\kappa})\big]\,\frac{\partial}{\partial a_\iota}\,[\nu(x_{\mathbf{r},\kappa'})]-$$

$$-\frac{1}{\sqrt{M'}\,\varrho_f\omega^2}\sum_{\kappa=1}^{M}b_\kappa\nu(x_{\mathbf{r},\kappa'})\cdot\mathrm{grad}_{\,x_{\mathbf{r},\kappa'}}\times$$

$$\times\big[\mathrm{grad}_{\,x_{\mathbf{r},\kappa'}}G(x_{\mathbf{r},\kappa'},x_{i,\kappa})\big]\,\frac{\partial}{\partial a_\iota}[x_{\mathbf{r},\kappa'}]-$$

$$-\frac{1}{\sqrt{M'}\,\varrho_f\omega^2}{}^{\top}\big[\mathrm{grad}_{\,x_{\mathbf{r},\kappa'}}p^{inc}(x_{\mathbf{r},\kappa'})\big]\,\frac{\partial}{\partial a_\iota}\,[\nu(x_{\mathbf{r},\kappa'})]-$$

$$-\frac{1}{\sqrt{M'}\,\varrho_f\omega^2}\,\nu(x_{\mathbf{r},\kappa'})\cdot\mathrm{grad}_{\,x_{\mathbf{r},\kappa'}}\times$$

$$\times\big[\mathrm{grad}_{\,x_{\mathbf{r},\kappa'}}p^{inc}(x_{\mathbf{r},\kappa'})\big]\,\frac{\partial}{\partial a_\iota}\,[x_{\mathbf{r},\kappa'}].$$

References

1. M. Abramowitz and A. Stegun, Handbook of mathematical functions with formulas, graphs, and mathematical tables. *National Bureau of Standards Applied Mathematics Series,* 55 *For sale by the Superintendent of Documents, U.S. Government Printing Office, Washington, D.C.*, 1964.
2. A. H. Barnett and T. Betcke, Stability and convergence of the method of fundamental solutions for Helmholtz problems on analytic domains. *J. Comput. Phys.* **227** (2008), No. 14, 7003–7026.
3. D. Colton and R. Kress, Inverse acoustic and electromagnetic scattering theory. Second edition. *Applied Mathematical Sciences,* 93. *Springer-Verlag, Berlin*, 1998.
4. J. Elschner, G. C. Hsiao, and A. Rathsfeld, An inverse problem for fluid-solid interaction. *Inverse Probl. Imaging* **2** (2008), No. 1, 83–119.
5. J. Elschner, G. C. Hsiao, and A. Rathsfeld, An optimization method in inverse acoustic scattering by an elastic obstacle. *SIAM J. Appl. Math.* **70** (2009), No. 1, 168–187.
6. M. A. Golberg and C. S. Chen, Discrete projection methods for integral equations. *Computational Mechanics Publications, Southampton*, 1997.
7. Ch. Hafner, The generalized multipole technique for computational electromagnetics. *Artech House Books, Boston*. 1990.
8. T. Hargé, Valeurs propres d'un corps elastique. *C. R. Acad. Sci. Paris Ser. I Math.* **311** (1990), No. 13, 857–859.
9. J. Hoffmann, Ch. Hafner, P. Leidenberger, J. Hesselbarth, and S. Burger, Comparison of electromagnetic field solvers for the 3D analysis of plasmonic nanoantennas. In: *Modeling Aspects in Optical Metrology II*, Eds.: H. Bosse, B. Bodermann, and R. M. Silver. *Proceedings of SPIE* **7390** (2009), pp. 73900J-1–73900J-11.
10. G. C. Hsiao, R. E. Kleinman, and G. F. Roach, Weak solutions of fluid-solid interaction problems. *Math. Nachr.* **218** (2000), 139–163.
11. G. C. Hsiao and W. L. Wendland, Boundary integral equations. Applied Mathematical Sciences, 164. *Springer-Verlag, Berlin*, 2008.
12. A. Kirsch and N. Grinberg, The factorization method for inverse problems. *Oxford Lecture Series in Mathematics and its Applications,* 36. *Oxford University Press, Oxford*, 2008.
13. A. Kirsch and R. Kress, An optimization method in inverse acoustic scattering (invited contribution). *Boundary elements IX, Vol. 3 (Stuttgart, 1987)*, 3–18, *Comput. Mech., Southampton*, 1987.
14. M. Lourakis, http://www.ics.forth.gr/∼lourakis/levmar
15. O. Ivanyshyn, R. Kress, and P. Serranho, Huygens' principle and iterative methods in inverse obstacle scattering. *Adv. Comput. Math.* **33** (2010), No. 4, 413–429.
16. A. Márquez, S. Meddahi, and V. Selgas, A new BEM-FEM coupling strategy for two-dimensional fluid-solid interaction problems. *J. Comput. Phys.* **199** (2004), No. 1, 205–220.
17. P. Monk and V. Selgas, An inverse fluid-solid interaction problem. *Inverse Probl. Imaging* **3** (2009), No. 2, 173–198.
18. D. Natroshvili, S. Kharibegashvili, and Z. Tediashvili, Direct and inverse fluid-structure interaction problems. Dedicated to the memory of Gaetano Fichera (Italian). *Rend. Mat. Appl. (7)* **20** (2000), 57–92.
19. D. Natroshvili, G. Sadunishvili, and I. Sigua, Some remarks concerning Jones eigenfrequencies and Jones modes. *Georgian Math. J.* **12** (2005), No. 2, 337–348.
20. J. Nocedal and S. J. Wright, Numerical optimization. Springer Series in Operations Research. *Springer-Verlag, New York*, 1999.
21. R. Potthast, Point sources and multipoles in inverse scattering theory. *Chapman & Hall/CRC Research Notes in Mathematics,* 427. *Chapman & Hall/CRC, Boca Raton, FL*, 2001.

22. O. Schenk, K. Gärtner, and W. Fichtner, Efficient sparse *LU* factorization with left-right looking strategy on shared memory multiprocessors. *BIT* **40** (2000), No. 1, 158–176.
23. J. Schöberl, NETGEN: An advancing front 2D/3D-mesh generator based on abstract rules. *Comput. Vis. Sci.* **1** (1997), No. 1, 41–52.
24. Y. X. You, G. P. Miao, and Y. Z. Liu, A numerical method for an inverse transmission problem. *Inverse Problems* **17** (2001), No. 3, 421–435.
25. A. Zinn, The numerical solution of an inverse scattering problem for time-harmonic acoustic waves. *Inverse problems and imaging* (*Glasgow,* 1988), 242–263, Pitman Res. Notes Math. Ser., 245, *Longman Sci. Tech., Harlow*, 1991

(Received 8.11.2010)

Authors' addresses:

J. Elschner and A. Rathsfeld

Weierstrass Institute for Applied Analysis and Stochastics
Mohrenstr. 39, 10117 Berlin
Germany
E-mail: elschner@wias-berlin.de
rathsfeld@wias-berlin.de

G. C. Hsiao

University of Delaware
Department of Mathematical Sciences
Newark, Delaware 19716–2553
USA
E-mail: hsiao@math.udel.edu